CHARLES UNIVERSITY

Faculty of Science

Study program: Clinical and toxicological analysis

Branch of study: Clinical and toxicological analysis

Sidónia Molitorisová

Stabilization of metal nanoparticles in MWW zeolite for catalytic applications

Stabilizácia kovových nanočastíc v zeolite MWW pre katalytické aplikácie

Bachelor thesis

Supervisor : Mgr. Mariya Shamzhy, Ph.D.

Prague 2021

Prehlásenie

Prehlasujem, že som túto záverečnú prácu spracovala samostatne a uviedla všetky použité informačné zdroje a literatúru. Táto práca ani jej podstatná časť nebola predložená na získanie iného alebo rovnakého akademického titulu.

Som si vedomá toho, že prípadné využitie výsledkov získaných v tejto práci mimo Univerzitu Karlovu je možné len po písomnom súhlase tejto univerzity.

V Prahe dňa 17.06.2021

Acknowledgement

I would like to thank my supervisor Mgr. Mariya Shamzhy, Ph.D. for her professional and patient guidance, support and time during my research. Furthermore, I would like to express my sincere gratitude to my advisors Maksym Opanasenko, Ph.D. for his useful instructions and prof. Ing. Jiří Čejka, DrSc. for advice and opportunity to work in his research group. I also want to thank all of my colleagues for their help and advice with measurements, namely Mgr. Ondřej Veselý, Mgr. Milan Eliáš, Ing. Martin Kubů, Ph.D. (nitrogen adsorption), Michal Mazur, Ph.D. and Ang Li, MSc. (STEM and EDS), Mgr. Kinga Maria Golabek, Ph.D. (FTIR), Ing. Jan Přech, Ph.D. (catalytic experiment and chemisorption) and Yuyan Zhang, MSc. (synthesis, catalytic experiment and evaluation).

Abstract

Controlling both size of metal nanoparticles (MNPs) and acidobasic characteristics of the zeolite support is highly desirable for preparation of stable and active bifunctional catalysts. 2D-3D transformation of layered zeolite precursor into three-dimensional zeolite coupled with metal encapsulation is one of the most efficient synthetic strategies so far to achieve the appropriate metal dispersion and aggregative stability of MNPs within zeolite matrix. Nevertheless, the effect of support acidic characteristics on the properties of thus prepared metal@zeolite catalyst remained unrevealed, while the synthetic strategy itself requires further optimization to minimize the loss of metal component. This work addresses the influence of chemical composition of zeolite layered precursor on physical-chemical and catalytic properties of metal@zeolite catalysts prepared *via* 2D-3D transformation strategy, taken Pd@MCM-22$_{2D\text{-}3D}$ system as a representative example. Both Si/Al ratio of MCM-22P layered precursor (e.g., Si/Al = 15, 20, 30) and Pd loading (e.g., 0.1, 0.3, 0.8 wt.%) were varied resulting in a set of nine Pd@MCM-22$_{2D\text{-}3D}$ catalysts. In addition, three Pd@MCM-22$_{impreg}$ catalysts with the same metal loading (0.1 wt.%), but different Si/Al ratios of a support were synthesized *via* conventional impregnation method and used as benchmarking materials. Thus, prepared Pd@MCM-22 catalysts were characterized by various techniques, such as XRD, nitrogen physisorption, electron microscopy, FTIR spectroscopy, while their catalytic performance was tested in hydrogenation of 3-nitrotoluene to 3-aminotoluene.

Key words: zeolites, metal nanoparticles, heterogeneous catalysts, material design

Abstrakt

Regulácia veľkosti kovových nanočastíc a acidobazických charakteristík zeolitového nosiča má zásadný význam pre prípravu stabilných a aktívnych bifunkčných katalyzátorov. 2D-3D transformácia vrstevnatého prekurzora zeolitu v trojromernú štruktúru spojená s uzavretím kovových nanočastíc do kanálového systému zeolitu je jedna z najefektívnejších syntetických metód doposiaľ zaznamenaná. Touto 2D-3D transformáciou je možné dosiahnuť vhodnú disperziu kovových nanočastíc, ako aj ich stabilitu voči agregácii. Účinok kyslých charakteristík zeolitického nosiča na vlastnosti nanesených kovových katalyzátorov však nebol skúmaný, zatiaľ čo vývoj syntézy vyžaduje optimalizáciu a zdokonaľovanie pre predídenie strát kovovej zložky. Táto práca sa zameriava na riešenie vplyvu chemického zloženia vrstevnatého prekurzoru zeolitu na fyzikálno-chemické a katalytické vlastnosti naneseného kovového katalyzátoru pripraveného stratégiou 2D-3D transformácie, pričom ako reprezentatívny príklad je zvolený Pd@MCM-$22_{2D\text{-}3D}$ systém. Variácia Si/Al pomeru MCM-22P vrstevnatého prekurzoru (konkrétne Si/Al = 15, 20, 30) a obsah Pd (konkrétne 0.1, 0.3, 0.8 hmotnostných percent) viedla k tvorbe deviatich Pd@MCM-$22_{2D\text{-}3D}$ katalyzátorov. Okrem spomínaných katalyzátorov boli nasyntetizované tri Pd@MCM-22_{impreg} katalyzátory s obsahom Pd 0.1 hm. % a Si/Al pomermi 15, 20, 30 pomocou konvenčnej impregnačnej metódy a boli použité ako referenčné materiály. Takto pripravené katalyzátory Pd@MCM-22 boli charakterizované rôznymi metódami, ako XRD, fyzisorpcia dusíka, elektrónová mikroskopia a FTIR spektroskopia. Ich katalytická účinnosť a aktivita bola testovaná v modelovej reakcii – hydrogenácia 3-nitrotoluénu na 3-aminotoluén.

Kľúčové slová: zeolity, kovové nanočastice, heterogénne katalyzátory, design materiálov

Table of contents

List of abbreviations

a.u.	arbitrary unit
BAS	Brønsted acid site
BBU	basic building unit
BET	Brunauer, Emmett and Teller theory
CBU	composite building unit
CTMA-Cl	cetyltrimethylammonium chloride
CTMA-OH	cetyltrimethylammonium hydroxide
EDA	ethylendiamine
EDS	energy-dispersive spectroscopy
EtOH	ethanol
FTIR	Fourier-transform infrared spectroscopy
GS-MS	gas chromatography mass spectrometry
HMI	hexamethyleneimine
ICP-MS	inductively coupled plasma mass spectrometry
IR	infrared spectroscopy
IUPAC	International Union of Pure and Applied Chemistry
IZA-SC	Structure Commission of the International Zeolite Association
LAS	Lewis acid sites
MNP(s)	metal nanoparticle(s)
rpm	rotations per minute
RT	room temperature
S_{BET}	specific surface area
S_{ext}	external surface area
SBU	secondary building unit
SDA	structure directing agent
SEM	scanning electron microscopy
Si/Al	silicon to alumina molar ratio
STEM	scanning transmission electron microscopy
TAA^+	tetraalkyl ammonium cation

TEM	transmission electron microscopy
TEOS	tetraethyl orthosilicate
TOS	time-on-stream
TPD	temperature programmed desorption
T^{3+}	trivalent element
T^{4+}	tetravalent element
V_{mes}	mesopore volume
V_{mic}	micropore volume
V_{tot}	total pore volume
XRD	X-ray powder diffraction
2D	two-dimensional
3-AT	3-aminotoluene
3D	three-dimensional
3-NT	3-nitrotoluene
ε(*BAS*)	molar absorption coefficient for Brønsted acid sites
ε(*LAS*)	molar absorption coefficient for Lewis acid sites

1. Introduction

Controlling the size of metal nanoparticles (MNPs) is crucial for their catalytic performance as the number of exposed active sites increases with decrease in the size of MNPs. Recent advances in synthesis of nanoporous materials have enabled to stabilize MNPs in their system of void channels and cages, that prevents sintering of metal nanoparticles. One of the possible supports are zeolites, crystalline aluminosilicates with versatile catalytic functions. Zeolites show acid sites, catalysing different reactions. Incorporation of noble metal nanoparticles such as Pd or Pt into zeolite pores provides high-performance and shape-selective bi-functional catalysts, bearing both acid and metal active centres.

Incorporation of metal nanoparticles into zeolites can be achieved by classical ion-exchange or impregnation. Recently an efficient method for encapsulation of Pt and Pd into MWW silica zeolite support was described in the literature. The method (designated here as '2D-3D incorporation') includes (1) swelling of 2D layered zeolite with cationic surfactant combined with metal precursor intercalation and (2) 2D-to-3D zeolite transformation. Despite good dispersing and stabilization of metal nanoparticles in zeolite matrix were achieved, the effect of zeolite chemical composition on the physical-chemical and catalytic properties of Pd@MWW catalysts prepared *via* '2D-3D incorporation' was not addressed, thus precluding design of bifunctional catalysts with variable concentration of acid sites. Moreover, the amount of a noble metal in metal@MWW catalysts was significantly lower *vs.* the amount used for encapsulation, evidencing that only part of the loaded metal was efficiently intercalated in zeolite interlayer space upon swelling.

This bachelor thesis aims at addressing an effect of chemical composition of a zeolite support (i.e., Si/Al ratio) on the physical-chemical and catalytic properties of Pd-supported MWW zeolites, while optimizing synthesis protocol for '2D-3D incorporation' to increase the efficiency of metal loading.

Thus, the main objectives of the bachelor thesis are:

- to synthesize aluminosilicate 2D and 3D MWW zeolites with different Si/Al ratios;
- to introduce Pd into MWW zeolite by 1) conventional impregnation method or by 2) metal encapsulation during 2D-to-3D transformation of layered zeolite precursor, modified by separation of swelling and metal impregnation steps in time;

- to characterize structural properties of the prepared Pd-supported zeolites using X-ray diffraction, nitrogen ad-/desorption, electron microscopy, infrared spectroscopy and chemical analysis;
- to evaluate activity and selectivity of Pd-supported zeolite catalysts in the model reaction of 3-nitrotoluene hydrogenation to 3-aminotoluene.

2. Theoretical part

2.1. Zeolites

Zeolites, crystalline microporous aluminosilicates with the highly organized framework structure, are broadly used in industry as sorbents and catalysts. Term zeolite (from the Greek *zeo* = to boil and *lithos* = stone) was firstly described in 1756 by Swedish mineralogist Axel Cronstedt for mineral stilbite found in a copper mine. The term interprets a reversible adsorption of water, one of the relevant properties of a zeolite. Zeolites together with other porous solids, such as sulphides or phosphates, are a part of the group of materials called molecular sieves, all characterized by pore sizes of molecular dimension.[1]

Nowadays, there are 253 types of zeolites approved by the Structure Commission of the International Zeolite Association (IZA-SC). Each zeolite type is represented by a three-letter code.[2]

The group of natural zeolites originates mainly from the volcanic and sedimentary processes and is not so greatly represented as synthetic zeolites, prepared in the lab as discussed in Section 2.1.4. The prominent representatives of natural zeolites with a wide range of applications in adsorption, ion-exchange and separation are chabazite, mordenite, clinoptilolite.[3] They are found in hydrated form, water molecules are located in cavities or channels, sometimes also forming aqueous bridges between atoms of a framework and exchangeable ions. Natural zeolites have reached a great success in environmental field of industry, especially in water treatment due to their ability to uptake organic or heavy-metal ions as contaminants. The modification by acid/base treatment could be applicated to improve the properties of natural zeolites.[4]

2.1.1. Structure

The framework of a zeolite is composed of tetrahedra TO_4 units (where T represents tetrahedral atom of Al or Si), connected through a shared oxygen bridge. Polymerization of basic tetrahedral building units (BBU) assembles higher arrangements - secondary building units (SBU).[1] A zeolite can be described according to the SBUs constituting its structure, although building units more complex than SBUs can be used for structural consideration. Composite building units (CBU) are nowadays used for structural description of a zeolite, containing features as cages or chains. Figure 1 shows the examples of the most frequent SBUs and CBUs found in zeolites.[5]

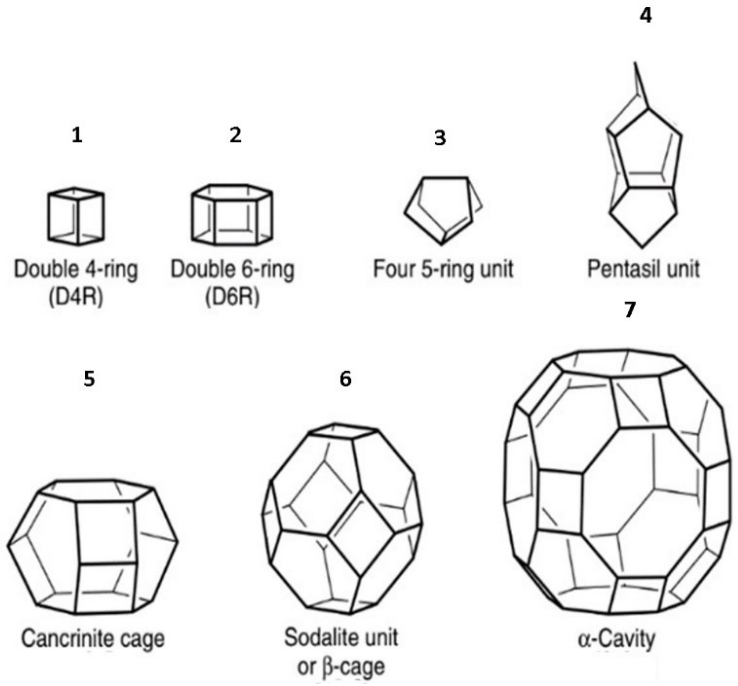

Figure 1: The most common SBUs (1-3) and CBUs (4-7) with their descriptive names [6]

Due to the presence of $[AlO_4]^-$ units, framework holds a negative charge compensated by alkali or alkaline-earth metal cations such as K^+, Na^+, Ca^{2+}, proton or organic (e.g., TAA^+) cations. In general, chemical composition of aluminosilicate zeolite is given by formula:

$$M^{b+}_{a/b}\,[(AlO_2)^-_a\,(SiO_2)_y]\cdot cH_2O \qquad (1)$$

where M represents exchangeable metal cation, b represents the charge of metal cation, c is the amount of water per unit cell and (a + y) represents the total number of the $[SiO_4]$ and $[AlO_4]^-$ tetrahedra in a unit cell.[7]

The similarity in T-O bond lengths and T-O-T bond angles of T = Al^{3+} or Si^{4+} makes Al^{3+} an ideal substituent of Si^{4+} in zeolites.[8] Besides Al, other heteroatoms (i.e., Ti, Sn, Ge, Ga) can be used for substitution of Si in a zeolite framework by so-called isomorphous substitution. Isomorphous substitution does not affect the structure of a zeolite, but modifies its chemical composition.[9] Such substitution is possible for atoms with electronegativity and size similar to those of Al and Si. Common trivalent elements are Ga, Fe or B, while Ti , Ge and Sn stand for tetravalent heteroatoms.[8] Acidic and catalytic properties of material itself are strongly dependent on the nature of substituting elements.

In contrast to 3D zeolites characterized by three-dimensional frameworks, zeolites defined as layered ones are formed of 2D sheets with thickness of only 2~3 nm (similar to

the size of unit cell). Crystalline zeolite layers are interacting *via* van der Waals forces or hydrogen bonds between silanol groups, while the integrity of the layers is ensured by strong covalent bonds, as it is shown for 2D and 3D MWW zeolites in Figure 2.

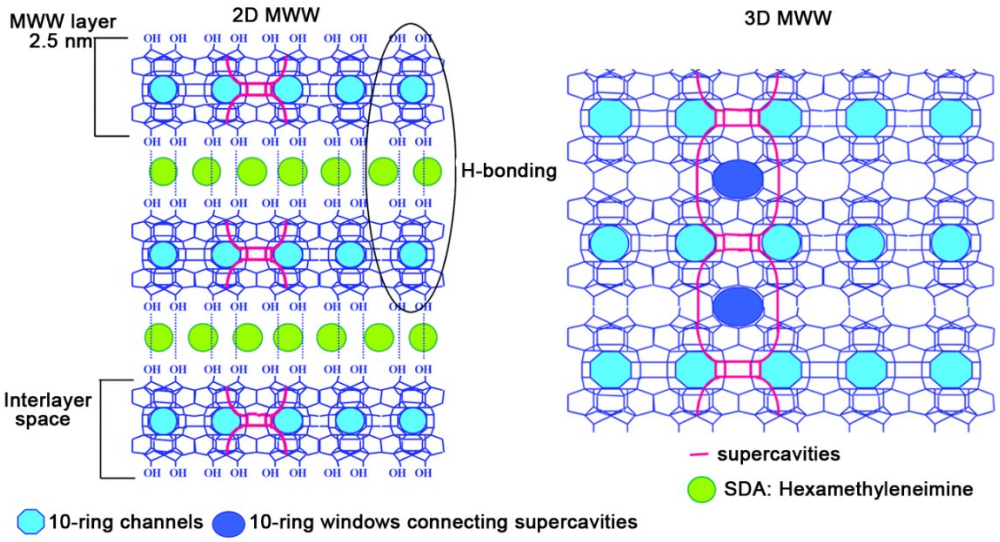

Figure 2: 2D and 3D MWW zeolites´ structures[10]

2.1.2. Pore system

The framework of a zeolite contains a system of size-differing cages and channels (pores) of molecular dimensions. Each pore opening is specified by the number of T-atoms (or, alternatively, to the number of O-atoms) in a ring. Based on the largest pore openings in a particular zeolite, zeolites are distinguished as[5]:

- **small pore zeolites** (e.g., ANA, CHA, GIS[11]) with channels limited by 8 T-atoms (diameter ~ 4.0 Å);
- **medium pore zeolites** (e.g., EUO, ITH, ITR, MFI, MWW[11]) with channels limited by 10 T-atoms (diameter ~ 5.5 Å);
- **large pore zeolites** (e.g., BEA, FAU, MTW, MOR[11]) with channels limited by 12 T-atoms (diameter ~ 7.0 Å);
- **extra-large pore zeolites** (e.g., CFI, DON, UTL [11]) with channels composed of >12 T-atoms (diameter > 7.0).

Zeolites can have 1-, 2- or 3-dimensional pore systems. A one-dimensional pore system (zeolites AFI, CFI, EUO) lacks intersection of particular channels, 2D (MWW, FER) or 3D systems (BEA) have intersection of channels in two or three dimensions, respectively.[1]

For some zeolites, cavities can be found in place of channel intersections, with their size bigger than the diameter of pore entrance.[1] For example, MWW zeolite features super-cavity of size 0.71x1.82 nm connected by 10-ring windows (Figure 2). Many characteristics of zeolites, such as adsorption properties and shape-selectivity, discussed in Section 2.1.5, are determined, in particular, by above-mentioned characteristics of the pore system.[6]

2.1.3. Brønsted and Lewis acid sites

Negative charge of zeolite framework formed upon incorporation of trivalent atom and its compensation by proton results in Brønsted acid sites (BAS), which are bridging hydroxyl groups $\equiv T^{3+}$-(OH)-Si$\equiv$ (T^{3+} = Al, B, Ga, Figure 3). The BAS can provide or donor proton when interaction with basic molecule occurs.[12] Concentration and type of trivalent atom in a framework influences density and strength of BAS, respectively.[8]

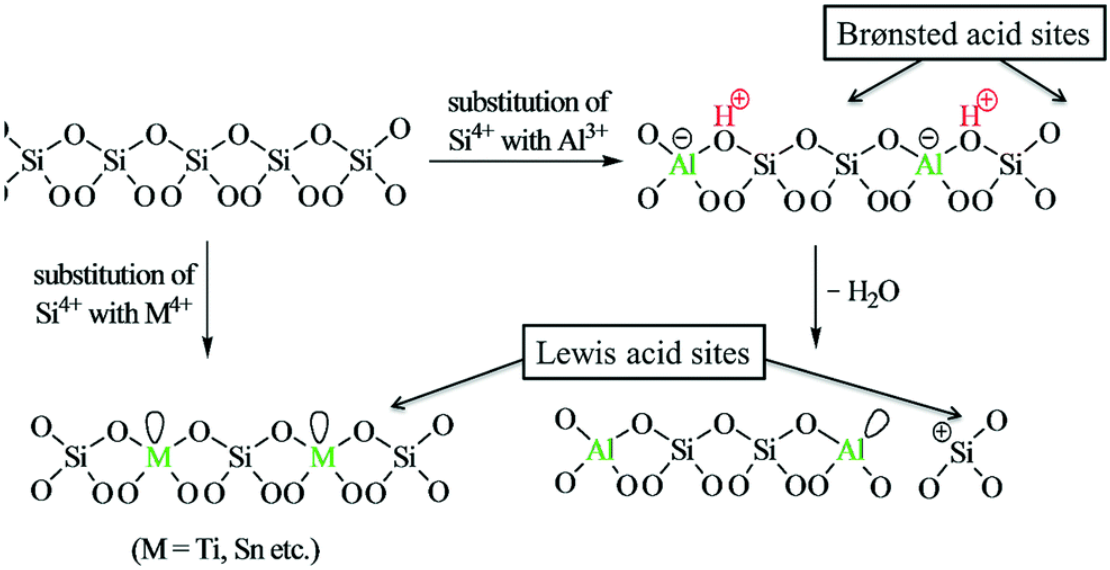

Figure 3: Brønsted and Lewis acid sites in zeolites[13]

By substitution of Al or Si with tetravalent metal atoms (usually Ti or Sn) or by dihydroxylation of BAS, electron-acceptor Lewis acid sites (LAS) are produced. The lowest unoccupied orbitals of tetravalent metal atoms are responsible for their Lewis acidity. Both Brønsted and Lewis acid sites can serve as catalytically active sites in zeolites.[7] BAS and LAS can be located on the external surface (external acid sites) of zeolite, but mostly in the pores (internal acid sites).[6]

2.1.4. Synthesis

The majority of zeolites is prepared synthetically *via* hydrothermal crystallization, either from natural raw sources (such as boehmite[14]) or synthetic materials (such as tetraethyl-

orthosilicate, aluminum isopropoxide and others). By varying the synthesis conditions or post-synthesis modifications, many characteristics of zeolites can be altered (e.g., structure type, chemical composition, size of the crystals) to design their properties for specific application.[3]

2.1.4.1. Hydrothermal synthesis of 3D zeolites

Hydrothermal synthesis is the mostly used method for the preparation of zeolites. Temperature for synthesis ranges 100 °C – 200 °C and pressure is above 1 bar.

Zeolite formation begins with induction period, time from the start of the reaction to the first appearance of zeolite nuclei (Figure 4). During the induction period, the initial interaction of reactants leads to the formation of primary amorphous species, which then agglomerate to form amorphous particles. In the nucleation step, amorphous particles crystallize to form zeolite nuclei, which is followed by crystal growth period.[15]

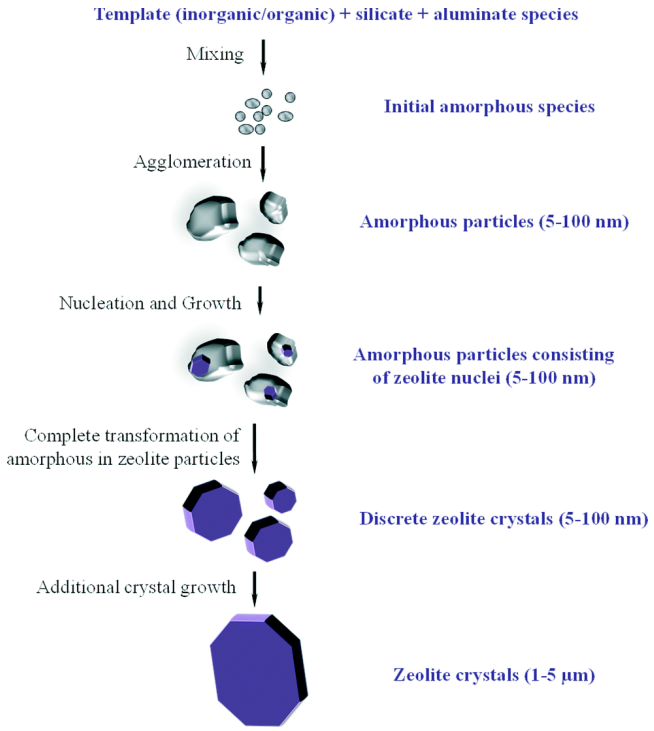

Figure 4: Zeolite crystallisation mechanism according to Ref. [16]

There are several parameters crucial for formation of zeolites:

- Source of framework elements

The choice of silica or alumina source can influence the rate and phase selectivity of zeolite crystallization. Commonly used silica sources are tetraethyl orthosilicate (TEOS), colloidal or fumed silica, sodium and potassium silicates. Suitable alumina reagents are aluminium

hydroxide, sodium and potassium aluminates, or alumina salts (sulphates, nitrates, chlorides).[5]

- Water concentration

Water provides suitable medium for solubility and transport of all components needed for the formation of zeolite. It plays important role in mediation of condensation process of Si and Al sources at all steps of crystallization process.[5]

- Mineralizing agents

The role of mineralizing agent, such as hydroxide and fluoride ions,[5] is to dissolve the sources of framework T-elements and to transform them to reactive state for further formation of T-O-T bonds of zeolite framework. The concentration of hydroxides (basic pH) needs to be properly chosen to ensure the solubility of silica and alumina species in medium.

- Structure-directing agents

SDAs, structure-directing agents, are mostly organic amines or tetraalkylammonium hydroxides whose function is to stabilize the forming zeolite framework by van der Waals and Coulombic interactions, while fulfilling the void volume of zeolite channels and cages. SDA promotes oligomerization of elementosilicate anions into particular structural subunits (zeolite nuclei).[17] Nature of cations influences the chemical composition of a framework in terms of Si/T^{3+} ratio. Usually, small-size inorganic cations promote the formation of Al-rich zeolites, as large number of such cations can fit zeolite voids to compensate the negative charge of the framework. Contrarily, the number of bulky organic cations is limited by the void space of a zeolite, hence the use of such cations is favourable for increasing Si/Al ratio of a zeolite.[5]

- Effect of time, temperature, pH

Temperature-pressure settings has an influence on crystallization rate affecting depolymerization of the sources of framework building elements and condensation processes involving the formed ions. Increasing the temperature is usually accompanied with an increase in both the rate of nucleation and crystal growth.[18] The pH of solution effects the final Si/Al ratio – increasing pH usually results in crystallization of low-silica zeolites.[1] The time of crystallization is an important parameter, as the formation of particular zeolite involves transformations between different metastable zeolitic structures and ends up with the most thermodynamically stable one, quarz.[19]

- Technical arrangement

The apparatus for hydrothermal synthesis is represented by sealed vessels, which have to handle high pressure generated at elevated temperature.[6] Commonly, Teflon-lined steel autoclaves are used. Teflon has an advantage of being mechanically and thermally stable and inert, thus not interacting with reaction mixture. The stirring is crucial for providing homogeneity of reaction mixture.

2.1.4.2. Post-synthesis modification of 2D zeolites: MCM-22P as a case example

Even though 3D zeolites are the commonly formed products of hydrothermal crystallization, in 1990s 2D MCM-22P, ordered layered precursor of MWW zeolite (Figure 2), was discovered to be formed upon hexamethylenediamine-assisted hydrothermal synthesis.[20] While MCM-22P was the first representative of the family of 2D zeolites, later on other zeolites (i.e., MFI,[21] FER [22]) were prepared. Totally, 13 of 253 known zeolites were synthesized in both 2D and 3D forms.[23] By various post-synthetic treatments including calcination, swelling and pillaring, the interlayer space of 2D zeolite precursors can be modified thus generating structures with different layer arrangement (Figure 5). It happens so by breaking the interlayer H-bonds, while the original integrity of the layer is remained.

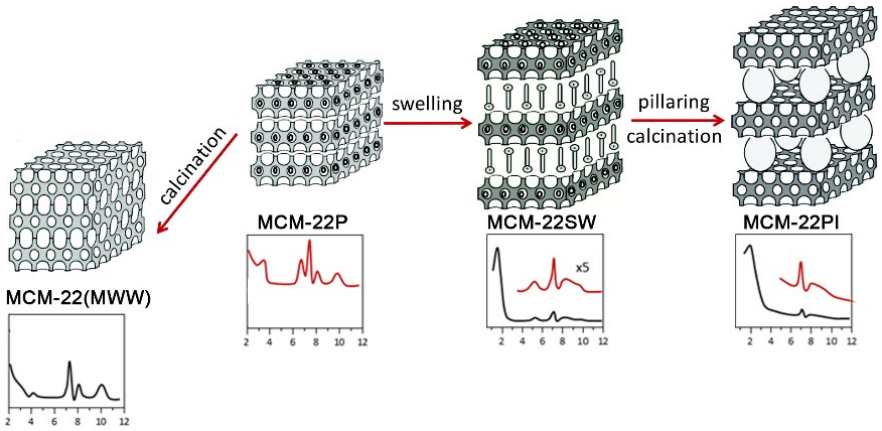

Figure 5: Schematic representation and XRD patterns of daughter materials prepared by post-synthesis modification of MCM-22P layered precursor of MWW zeolite[24]

- Calcination is the process when organic surfactant/SDAs are eliminated and condensation of terminal Si-OH groups to form Si-O-Si bonds occurs, what creates 3D structure.[20] Calcination of MCM-22P layered precursor results in 3D MWW zeolite, as observed from the XRD patterns of respective materials (Figure 5).

- Swelling refers to the expansion of interlamellar space by incorporation of organic cationic surfactant between layers. Swelling is performed in basic environment to break the interlayer hydrogen bonds between silanol groups. Successful swelling is shown in XRD pattern, where small peak in the region <3 °θ is apparent, revealing the expansion of layers.[25] In the case of MCM-22P, the commonly used swelling agent is CTMA-OH, cetyltrimethylammonium hydroxide.[26] Content of aluminium in MCM-22P was shown to play a decisive role for efficiency of swelling process – with increasing content of aluminium, the more severe conditions (higher pH and temperature) are needed to achieve a complete swelling of MCM-22P.[5] Swelling allows further modifications of material towards permanently expanded layers *via* pillaring.
- Pillaring is defined as ''*process by which a layered compound is transformed into a thermally stable micro- and/or mesoporous material with the retention of the layer structure*.''[27] Firstly, the swollen material is treated with mostly used inorganic pillaring agent TEOS. This is followed by calcination to release organics and build up amorphous silica pillars *via* condensation of TEOS molecules.[5]

2.1.5. Useful properties and application

With their advantageous properties, such as uniform pore size, chemical variability, thermal stability, zeolites found the application in various areas of industry. The most significant area of use is heterogeneous catalysis. In catalytic process, zeolite activity largely depends on the nature and concentration of BAS and LAS, accessible for reactants. In turn, by varying the size and shape of zeolite channels, it is possible to tune selectivity of the catalyst, where

- only molecules with smaller size than the pores' size can diffuse through the channel system of a zeolite and transform into products on the internal active sites of the catalyst (this phenomenon refers to *reactant shape selectivity*, Figure 6);[28]
- only transition states smaller than voids of zeolites can be formed to enable particular path of reactants transformation (*restricted transition state shape selectivity*, Figure 6);
- only the products with the size not exceeding zeolite pore openings can diffuse off the catalyst's channels (*product shape selectivity*, Figure 6).

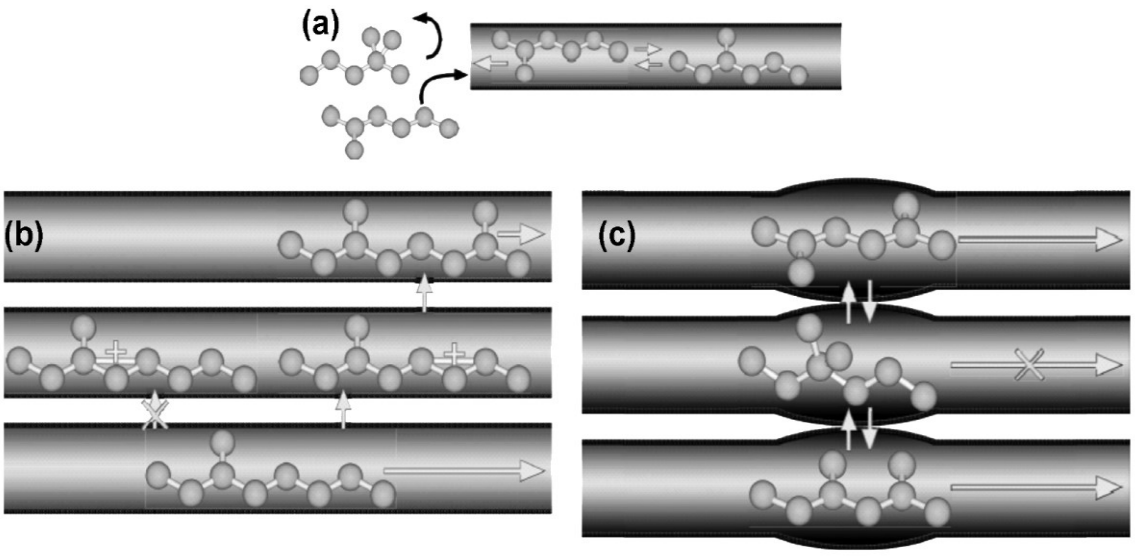

Figure 6: Shape selectivity in zeolite-catalysed reactions: reactant selectivity (a), restricted transition state selectivity (b) and product selectivity (c)[29]

The layered 2D zeolite catalysts have a great advantage of faster diffusion of reactant and product molecules.[30] Moreover, layered zeolites show enhanced accessibility of acid sites due to large external surfaces. Small thickness of crystalline layers provides high external surface area, thus uncovering the available active sites on external surface of the material.[31]

The adsorption properties of zeolites performing as molecular sieves provide their use in separation processes. The physical adsorption of adsorbate to the surface of adsorbent is mediated by weak van der Waals interactions, which can easily be broken by change in adsorption conditions. Desorption occurs, enabling the reuse of adsorbent (in this case zeolite) in virtually unlimited adsorption-desorption cycles.[5] Similarly to the selectivity and activity of zeolite catalyst, the size of the pores plays a crucial role in the effectiveness of adsorption.[32]

The presence of extra-framework cations in zeolites allows their use in ion-exchange processes. As ion-exchangers, zeolites are used in washing powders as detergents and the wastewater treatment to remove toxic contaminants. For its high cation exchange capacity, the natural zeolite clinoptilolite is used for the removal of ammonium ions from water.[33]

2.2. Metal-supported zeolites

Metal nanoparticles (MNPs) exhibit great catalytic performance in redox reactions, such as hydrogenation, hydroformylation, epoxidation and others. Under harsh conditions, the

stability of MNPs is decreasing and aggregates are formed, thus there is need for the support, which can provide the sufficient stabilization against sintering. Zeolites with their micropore channel system are ideal hosts for MNPs. The defined void size of zeolites restricts the growth of encapsulated MNPs thus enabling to control the dispersion of as-prepared metal-supported catalysts and to prevent severe aggregation of MNPs upon thermal treatment or the catalytic run.[34]

2.2.1. Preparation

Metal nanoparticles can be encapsulated into zeolites by 2 major ways - **in situ preparation** during zeolite hydrothermal synthesis and **post-synthesis modification** (i.e., impregnation, ion-exchange).[34]

- **In-situ method**, known as direct synthesis, is a procedure where metal precursor is one of the components of reaction mixture. Alkaline environment (pH>12) needed for zeolite crystallization causes metal precursor to precipitate thus hindering its encapsulation into zeolite voids.[35] To prevent aggregation of small MNPs during crystallization in alkaline medium, stabilization by ligands (N-ligands such as ethylenediamine, ammonia or S-ligands such as 3-mercaptopropyl[36]), which are soluble in basic aqueous environment is usually applied. The ligands are then removed by calcination in air and final metal catalyst is obtained by reduction in H_2 flow. The application of in-situ method is strongly limited by the necessity to develop protective agents capable to stabilize metal precursors against precipitation in alkaline medium.
- **Impregnation**, more precisely incipient wetness method, is the loading of zeolite with metal by mechanical mixing of zeolite with solution of metal source.[37] In this method, the volume of a solution used corresponds to the void volume of a zeolite support. For successful encapsulation of metal, the pores of zeolite are expected to be unoccupied without any organic templates, otherwise bulky metal aggregates located on the external surface can be formed. [38] Another crucial factor is metal loading, which should be optimized to reach homogeneous dispersion on the surface of a zeolite for the highest catalytic activity.[39]
- **Ion exchange** is based on replacement of alkali or alkali-earth framework compensating cations with transition metal cations using solutions of e.g. amine complexes ($[Pt(NH_3)_4](NO_3)_2$) as metal source. The lower Si/Al of the framework,

the higher ion exchange capacity is provided.[40] To ensure the required metal loading, ion exchange procedure needs to be repeated. The washing of a zeolite after each ion exchange with water leads to the huge loss of metal ions.[34] Thus, despite its simplicity, ion exchange method suffers from high metal consumption, which may be a severe drawback for the preparation of expensive noble metal-supported catalysts.

- **Transformation of 2D-to-3D zeolite with encapsulation of metal specie**s ('2D-3D incorporation') is a breakthrough method recently reported by Corma *et al*.[41] Layered precursor of 3D zeolite (specifically, MCM-22P) is swollen with organic surfactant solution containing Pt species. The calcination in air removed the swelling agent and resulted in the formation of 3D MWW framework with metal remained trapped in internal super-cages and on external surface as well. So prepared MNPs were shown to be thermally stable and highly catalytically active. While the pioneering work[41] used pure silica MCM-22 zeolite as a support of Pt nanoparticles, Ref.[42] reports on the encapsulation of Pd NPs in MCM-22 zeolite with Si/Al = 15. For both Pt and Pd, 2D-3D transformation method allowed the successful encapsulation of small MNPs into zeolite voids and their stabilization against sintering and aggregation, although inefficient impregnation of metal from swelling solution was observed in both cases as the noble metal content in a catalyst was 5-times lower in comparison to its theoretical loading. Thus, this work pursuit improving the efficiency of '2D-3D incorporation' method by separation of swelling and metal impregnation steps, as described in Section 3.3.2.

2.2.2. Characterization

The methods used for the characterization of metal-supported zeolite materials can be classified as follows: 1) the ones applied for characterization of zeolite support and 2) the ones used for the detailed analysis of metal nanoparticles. They are briefly summarized in Table 1 and discussed in detail in particular sub-sections.

Table 1: The most commonly used methods for characterization of metal@zeolites

Analysed entity	Method	Provided information	Reference
Zeolite support	X-ray diffraction	Phase purity and structure	43
	Physisorption	Textural properties	44
	FTIR spectroscopy of adsorbed pyridine	Nature and concentration of acid sites	45
	SEM	Shape and size of the zeolite crystals	46
	TEM	MNPs size distribution	46
Metal	Chemisorption of probe molecules, such as H_2, CO (e.g., pulse titration, TPD)	Concentration of exposed metal centres	47
	Model reaction	Activity, selectivity	36

2.2.2.1. X-ray diffraction

X-ray diffraction (XRD) is a characterization method used for the crystal structure refinement and phase identification. The method is based on interference of monochromatic X-rays scattered by a periodic arrangement of atoms with long-range order when conditions satisfy the Bragg's law:

$$\lambda = 2d_{hkl} \cdot \sin 2\theta \qquad (2)$$

where λ is the wavelength of the X-ray radiation, fixed in the most of diffractometers; 2θ is the angle of incidence; d_{hkl} is the vector drawn from the origin of the unit cell to intersect the crystallographic plane (hkl) at a 90° angle. The magnitude of d_{hkl} corresponds to the distance between parallel (hkl) planes of atoms (Figure 7).

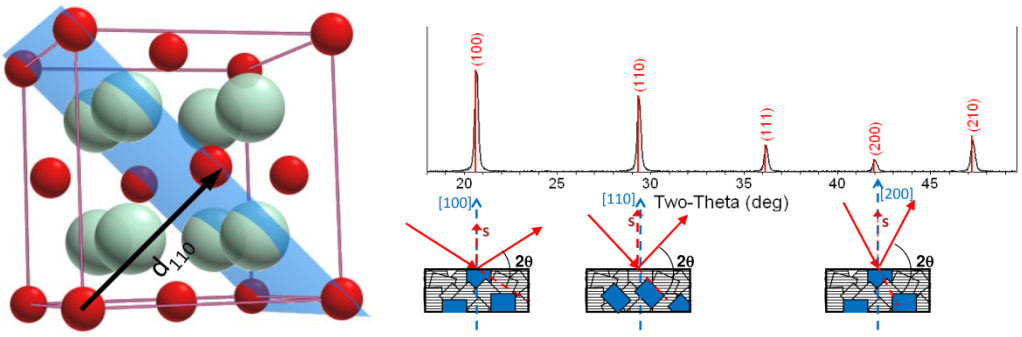

Figure 7 : The terms of the Bragg's law[48]

X-rays are electromagnetic radiations with short wavelengths around 0.5-2.5 Å, which is similar to the interatomic distances.[49] We differ between single crystal and powder X-ray diffraction (polycrystalline). In single crystal XRD, the diffraction pattern is visible as spots (Figure 8a), while in powder XRD, pattern is represented by rings (Figure 8b) due to the random orientations of crystallites and overlapping of the diffraction from the atomic planes of different crystals.[6]

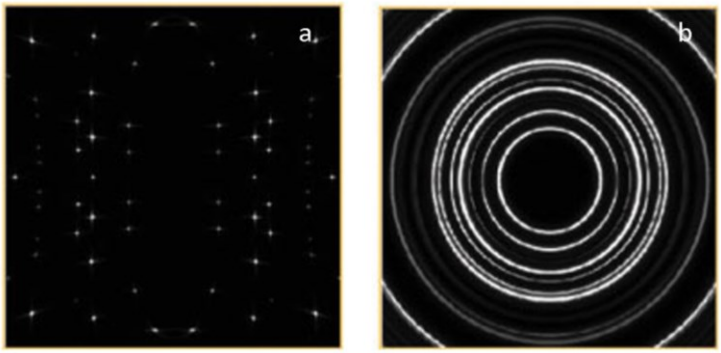

Figure 8 : X-ray diffraction patterns on single crystal (a) and polycrystalline (b) materials[50]

Measured diffractogram is unique for each zeolite. The standard way of identification is comparing obtained diffractogram with the ones collected in International Zeolite Association database.[2] Information found in diffractogram are peak positions, referring to the size and shape of a unit cell, peak widths related to the size of crystallites and intensities referring to the arrangement of atoms in the unit cell and their nature.[5]

2.2.2.2. Physisorption

Physisorption refers to the adhesion of the molecules of inert gases, such as Ar, N_2 (the adsorbate) on the surface of solid material (the adsorbent). Adsorption experiment is usually performed at the boiling point of the adsorptive gas. The adsorbate molecules interact weakly

with adsorbent surface (through van der Waals, quadrupole or dipole interactions), what makes physisorption reversible. The adsorption isotherm represents the dependence of the adsorbate uptake on its partial pressure at constant temperature. The shape of the isotherm, the overlapping or separation of its adsorption and desorption branches reflect textural characteristics of the material, such as the size of the pores and the available void volume. Micropores, the pores with sizes limited by 2 nm, are filled (shown in Figure 9a) at low relative pressures and when the pores are fully filled, the saturation occurs, resulting in type I isotherms (Figure 9b). In mesoporous materials, having the pores with diameters in the range 2 – 50 nm, the multilayer adsorption takes place, as represented in type IV isotherm, usually featuring the hysteresis loop (Figure 9b). By analysing physisorption isotherms, textural properties of porous materials are characterized, such as surface area (by BET method), pore volume and pore size. For determining the textural properties in macropore range, method of mercury porosimetry is used.[44]

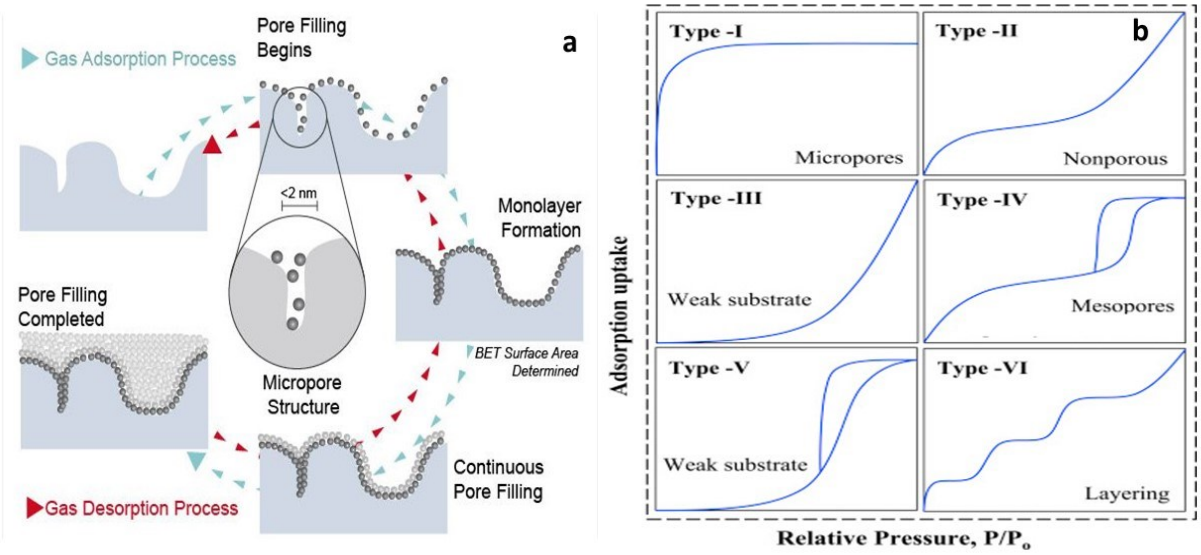

Figure 9: Physisorption in micropores and mesopores (a)[51] ; types of isotherms according to IUPAC classification (b)[52]

2.2.2.3. Fourier transform infrared spectroscopy

Infrared spectroscopy is a technique based on absorption of infrared light (wavelength 700 nm – 1 mm) in material. The interaction causes the population of vibrational levels of molecules to change due to the absorption of radiation at frequency matching the difference of vibrational levels. This gives rise to the infrared spectrum that is a function of IR light

intensity *vs.* its energy (e.g., frequency or wavelength). The interferogram after measurement in most cases undergoes Fourier transformation, leading to setup called FTIR spectroscopy. IR provides important information about type (qualitative analysis) and concentration (quantitative analysis) of acid sites in a zeolite. Investigation of Brønsted and Lewis acid centres is done by chemisorption of basic probe molecules (e.g., pyridine, acetonitrile, ammonia). The formation of H-bonded or coordinatively-bonded adduct of a probe molecule with acid sites gives rise to characteristic absorption bands in the FTIR spectrum. For example, the nature of acid sites in a zeolite can be determined based on the region 1700 – 1400 cm^{-1} when absorbing pyridine as probe molecule (see Figure 10):

- Lewis acid sites at 1448-1442 cm^{-1} (weak LAS) and at 1455 cm^{-1} (strong LAS)
- Brønsted acid sites at 1544 cm^{-1}
- intensive band at 1490 cm^{-1} as contribution of Brønsted and Lewis acid sites.

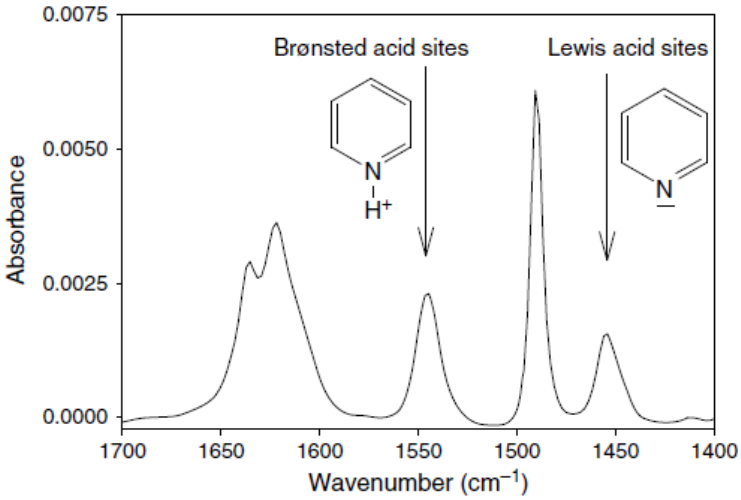

Figure 10: FTIR spectrum of pyridine adsorbed in a zeolite showing the bands characteristic of Brønsted and Lewis acid sites [6]

Temperature-programmed desorption of base probe molecule with FTIR monitoring is a method used to evaluate the strength of acid sites. With increasing temperature, decreasing intensities refer to decrease in a surface coverage. A higher temperature needed for releasing the probe molecule from the site indicates a higher acid strength of a particular centre. For probing the strength of acid sites in aluminosilicate zeolites with pyridine, the typically used temperatures are 150, 250, 350 and 450 °C.

2.2.2.4. *Electron microscopy*

Electron microscopy is a characterisation method enabling analysis of the size, shape and structure of the particles with a resolution of < 1 nm (SEM) or even < 0.05 nm (advanced TEM). In scanning electron microscopy (SEM), sample is analysed under the beam of electrons with energies of 1-30 keV generated from electron gun. Electrons can be absorbed, elastically scattered back or, by inelastic scattering, produced as secondary electrons while releasing the energy in a form of X-rays or luminescence.[5] Altogether, different types of electrons are analysed by detectors and provide qualitative information about the morphology, texture and surface topology (Figure 11a). In transmission electron microscopy (TEM), electrons are of higher energy (30-300 keV) and only thin specimen investigated (Figure 11b). TEM images have thus higher resolution than SEM and can provide visualization of zeolite pores and crystallite intergrowths. The high energy frequently causes the damage of the sample due to, e.g., overheating or ionization. TEM in combination with EDS (energy-dispersive spectroscopy) enabling elemental analysis is used for determination of size, shape, location and distribution of MNPs encapsulated in zeolite.[46]

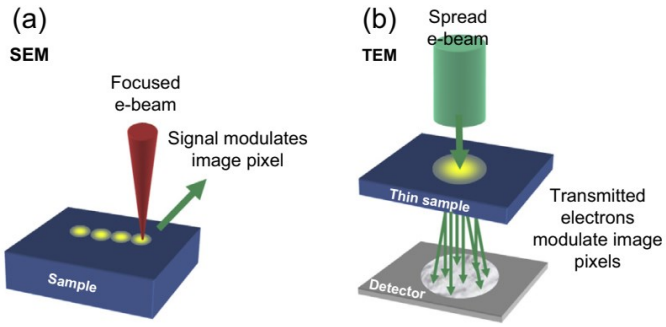

Figure 11: SEM and STEM imaging [53]

2.2.2.5. *Chemisorption*

Chemisorption, contrary to physisorption, involves the formation of chemical bonds between adsorbate molecule and an adsorptive site (in this case metal sites) of the adsorbent surface according to the chemical reaction stoichiometry (Figure 12a).[54] Thus, determination of the amount of chemisorbed molecules using, for example pulse titration approach (Figure 12b) is a facile way to assess the number of the atoms exposed on the surface of metal species, that is a small fraction of the overall metal atoms in the material available for the reacting molecules and serving as catalytically active sites.

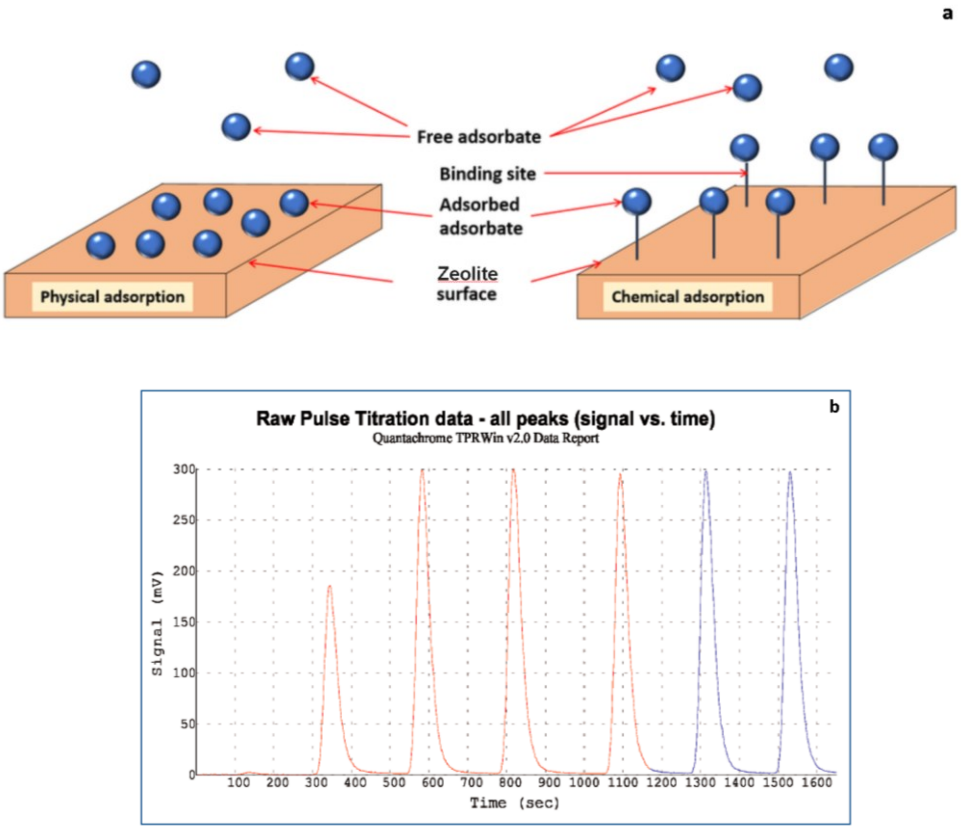

Figure 12: Surface non-specific physisorption and site-specific chemisorption (a)[55]; pulse titration of surface metal sites (b)[56]

For selective chemisorption on a surface of the most of noble and transition metals, carbon monoxide and hydrogen are used as those adsorbates do not interact significantly with the frequently used support material (e.g., silica, alumina, carbon), but form a chemical bond with a metal.[57]

Chemisorption results are used to calculate the dispersion of metal species, D (i.e., the fraction of exposed metal atoms) according to the following equation[58]:

$$D = \frac{n_{surface}^{metal}}{n_{total}^{metal}} = \frac{S \cdot n_{adsorbate}}{n_{total}^{metal}} \quad (3)$$

where

$n_{surface}^{metal}$ is the amount of metal atoms on the surface;

n_{total}^{metal} is the total amount of metal atoms on the surface and in the bulk;

S is the stoichiometry of chemisorption reaction referring to the mean number of surface metal atoms binding with a single molecule of an adsorbate at a monolayer coverage, e.g., Pd/CO chemisorption stoichiometry S is reported to be value of 2[59];

$n_{adsorbate}$ is the amount of adsorbate forming monolayer on the metal surface.

The results of chemisorption also allow to estimate the mean diameter of metal species, d_{Metal}, although the relation between d_{Metal} and dispersion is determined by the shape of metal NPs. For spherical NPs:

$$d_{Metal} = \frac{6 \cdot v_m}{a_m \cdot D} \quad (4)$$

where

v_m is the volume occupied by metal atom [cm^{-3}], $v_m = \frac{M}{\rho \cdot N_A}$ (M – molar weight [g/mol], ρ – metal density [g/cm^3], N_A – Avogadro's number);

a_m – the surface area occupied by a metal atom [cm^{-2}], $a_m = \frac{1}{n_{surface}^{metal}}$;

D – metal dispersion determined according to eq. (3).

2.2.2.6. Catalytic performance in a model reaction

Testing the catalyst activity, selectivity and stability in a model reaction is considered among the basic characterization methods of metal-supported catalysts.

Selective hydrogenation of nitroarenes provides aniline and its derivates, which are key-intermediates for pharmaceutical, agrochemical, dying and polymer industry.[60,61] The metal catalysts stand as important components in the reaction, allowing selective reduction of nitro group in the presence of different functional groups and full reduction through nitroso- and hydroxylamine- groups as intermediates to final amino group.[62] Moreover, the hydrogenation of nitroarenes to anilines (Figure 13) is a convenient model reaction frequently used for testing new metal catalysts. The dispersion of metal species on a support provides highly active and selective catalyst. However, metal aggregation at harsh working conditions can seriously deteriorate the catalyst performance due to the reduced fraction of exposed metal sites.

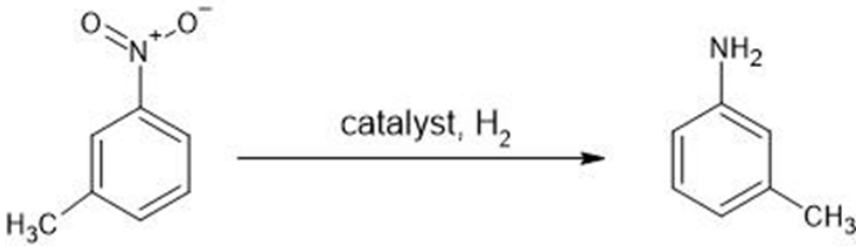

Figure 13: Hydrogenation of 3-nitrotoluene to 3-aminotoluene

Efficient encapsulation of metal NPs into zeolite voids, the main focus of this work, is expected to result in a high dispersion of metal species which will be reflected in enhanced catalytic activity of the designed catalysts in hydrogenation of 3-nitrotoluene (Figure 13) chosen as a model reaction.

3. Experimental part

3.1. List of used chemicals

For preparation of zeolite precursors and metal@zeolite catalysts, for their characterization and catalytic testing, chemicals listed in Table 2 were used.

Table 2: List of used chemicals

Chemical	Purity	Dealer
Ambersep 900(OH), ion exchange resin		Alfa Aesar
Ammonium nitrate	≥99%	Sigma Aldrich
Cetyltrimethylammonium chloride solution 25 wt.% in H_2O		Sigma Aldrich
Ethanol	99,8%	LACHNER
Ethylenediamine	≥99%	Sigma Aldrich
Hexamethyleneimine	99%	Sigma Aldrich
Hydrochloric acid	34-37%,	ANALPURE
Hydrofluoric acid	47-51%,	ANALPURE
Ludox LS colloidal silica 30 wt.% suspension in H2O		Sigma Aldrich
n-Dodecane	≥99,9%	MERCK
n-Hexane	100%	VWR CHEMICALS
Nitric acid	67-69%	ANALPURE
Palladium(II) acetate	99,9%	Sigma Aldrich
Pyridine	99,9%	Sigma Aldrich
Sodium aluminate		Sigma Aldrich
Sodium hydroxide	50%	MERCK
3-nitrotoluene	99%	Sigma Aldrich

3.2. Synthesis of MCM-22P and MWW zeolites

MCM-22P, the layered precursor of MWW zeolite, was prepared by hydrothermal synthesis. The synthetic gel was composed of Ludox LS-30 (colloidal silica, 30 wt.% suspension in water), $NaAlO_2$ (55% Al_2O_3, 45% Na_2O), NaOH (50% solution in water), HMI and distilled water. The composition of gel was varied as followed:

Si/Al = 15 30 SiO_2 : Al_2O_3 : 2.5 Na_2O : 10 HMI : 580 H_2O

Si/Al = 20 40 SiO_2 : Al_2O_3 : 2.5 Na_2O : 10 HMI : 580 H_2O

Si/Al = 30 60 SiO_2 : Al_2O_3 : 2.5 Na_2O : 10 HMI : 580 H_2O

Firstly, $NaAlO_2$ and NaOH were dissolved in distilled water. Ludox LS-30 and HMI were further added and the mixture was stirring for 2-3 hours at room temperature. The crystallization took place in the Teflon-lined autoclave under rotation (60 rpm) at T = 143 °C for 4 days. After completion of crystallization, autoclaves were cooled with water, the solid product was isolated by filtration, washed with distilled water until pH ≈ 7 and dried at T = 60 °C for one day. Thus prepared zeolites were named as MCM-22P(n), where n corresponds to Si/Al ratio in the reaction mixture.

To prepare 3D MCM-22 zeolites (designated here as MWW(n)), the respective layered MCM-22P(n) precursors were calcined in air flow at T = 540 °C for 6 hours with the heating rate 1 °C/min.

3.3. Synthesis of Pd@MWW

Pd@MWW(n) samples were prepared by 2 procedures – impregnation of 3D MWW(n) zeolites with Pd (the respective samples are designated as xPd@MWW(n)$_{impreg}$, where x is Pd loading in wt.%) and 2D-to-3D transformation of MCM-22P(n) layered precursors combined with Pd impregnation (the respective samples are designated as xPd@MWW(n)$_{2D\text{-}3D}$, where x is Pd loading in wt.%).

3.3.1. Impregnation of Pd into MWW

Framework compensating Na^+ cations in MWW(n) samples were firstly exchanged with NH_4^+ cations according to the following procedure. 1g of MWW(n) was treated with 50 ml 1M NH_4NO_3 at RT for 3 hours. Mixture was centrifugated, supernatant was removed, and solid sample was washed with distilled water 3 times. The tube was again filled with 50 ml 1M NH_4NO_3 and process was repeated 3 more times. The samples were then dried at T = 60 °C overnight.

For the impregnation of 0.1 wt.% Pd into MWW(n), solution of $Pd(en)_2(ac)_2$ was firstly prepared by mixing of 1 mg of $Pd(ac)_2$, 10 ml EtOH and 0.2 g EDA, followed by sonication for 5 min. Then, 1 g of each MWW(n)/NH_4^+ sample was mixed with the $Pd(en)_2(ac)_2$ ethanolic solution. The mixture was left stirring in open flask at room

temperature, until all EtOH was evaporated. After drying at RT, the samples were calcined in air flow at T = 540 °C for 6 hours, with a heating rate 1 °C/min. Final samples were marked as 0.1Pd@MWW(n)$_{impreg}$.

3.3.2. 2D-3D transformation of MCM-22P coupled with Pd impregnation

MCM-22P (n) samples were used as parent materials.

Swelling agent, the CTMA-OH solution, was prepared by mixing of 100 ml CTMA-Cl (25 wt.% in H_2O) with 70 g of ion-exchange resin Ambersep 900(OH) for 4 hours at RT, followed by removal of ion-exchange resin by filtration.

For swelling process, 2 g of MCM-22P(n) were mixed with 40 g of CTMA-OH solution at RT overnight. Samples were dried at RT until dry.

The next step was the preparation of $Pd(en)_2(ac)_2$ solution, which is described in detail in previous section. To prepare metal-supported zeolites with different metal loadings, swollen MCM-22(n) samples were treated with $Pd(en)_2(ac)$ solution of appropriate concentration at RT and left stirring in open flask overnight. 1, 3 or 8 mg of $Pd(ac)_2$ per 1 g of swollen MCM-22(n) was used to reach 0.1, 0.3 or 0.8 wt.% Pd loading, respectively. The solid samples were dried at RT and marked as MCM-22(n)/sw/xPd, where x corresponds to the wt.% of Pd loading. Calcination was performed in air flow at T = 540 °C for 6 hours with heating rate 1 °C/min. The final catalyst samples were named as xPd@MWW(n)$_{2D\text{-}3D}$.

3.4. Characterization of materials

Powder X-ray diffraction patterns were collected using Bruker D8 Advance diffractometer equipped with Linxeye XE-T detector, using CuKα (1.5406 Å) radiation. Analysed samples were firstly gently grinded and put into holder to prevent the preferential orientation of individual crystals.

Nitrogen adsorption/desorption isotherms measuremets were performed on a Micromeritics 3Flex volumetric Surface Area Analyzer at T = -196 °C. Before the sorption measurements, all samples were outgassed under the turbomolecular pump vacuum using a Micromeritics Smart Vac Prep instrument; starting at RT up to T = 110 °C with a heating rate 1 °C/min until the residual pressure of 13.3 Pa was achieved. After heating at T = 110 °C for 1 h, the temperature was increased to T = 250 °C (1 °C/min) and maintained for 8 hours. The specific surface area (S_{BET}) was calculated by the BET method[63,64] using adsorption data in the range of a relative pressure p/p_0 = 0.05-0.20. The *t*-plot method [65] was used to calculate

the micropores volume (V_{mic}) and external surface area (S_{ext}). The adsorbed amount at relative pressure $p/p_0 = 0.95$ reflects the total adsorption capacity (V_{tot}).

The Pd content and the Si/Al ratios of the catalysts were determined by ICP-MS analysis (Agilent 7900 ICP-MS; Agilent Technologies, Inc., USA). Ca 50 mg of the sample was mixed with 1.8 ml of HNO_3 (67-69%, ANALPURE®), 5.4 ml of HCl (34-37%, ANALPURE®), 1.8 ml of HF (47-51%, ANALPURE®), then transferred into a closed Teflon vessel, placed in the microwave (Speedwave® XPERT, Berghof) and heated at T = 210 °C (5 °C/min) for 25 min. After cooling down, the complexation of the surplus HF was performed by adding 12 mL of H_3BO_3, followed by further treatment in the microwave at T = 190 °C (5 °C/min) for 10 min. Finally, the obtained cooled down solutions were diluted for analysis.

FTIR spectroscopy was performed to investigate the acidity of samples by evaluating the concentration of Lewis and Brønsted acid sites. The measurement was performed at room temperature using Nicolet iS50 spectrometer with an MCT/B detector. The spectra were collected at spectral resolution of 4 cm^{-1} with 128 scans per single spectrum. The self-supporting wafers (density 10 mg/cm^2) were prepared by pressing the samples. The samples were firstly activated *in situ* at T = 450 °C for 4 hours in vacuum. Before each measurement, the background spectrum at room temperature was collected. Degassed pyridine as probe molecule was used for adsorption at T = 150 °C for 20 min, followed by desorption at T = 150; 250; 350 and 450 °C, each for 20 min. The concentration of LAS and BAS were calculated by integration of intensities of IR bands at 1454 cm^{-1} for LAS and 1545 cm^{-1} for BAS. The molar absorption coefficients used for calculation according to literature [66] were $\varepsilon(LAS) = 2.22$ cm/μmol and $\varepsilon(BAS) = 1.67$ cm/μmol.

Scanning transmission electron microscopy (STEM) measurements were performed using a JEOL JEM NEOARM-200F microscope operated at 200 kV. The samples were prepared by direct deposition on a copper holey carbon TEM grids. Images were collected in scanning mode using a JEOL annular dark-field and bright-field detectors. Energy dispersive X-ray spectroscopy (EDS) element distribution maps were acquired using a JEOL JED-2300 energy dispersive X-ray analyser.

Analysis of metal dispersion was performed at AMI-300 LITE chemisorption analyser. The sample was placed into U tube and stacked with quartz wool. Before measurement, the sample was pre-treated in-situ in 5% H_2 in Ar at T = 350 °C (5 °C/min)

for 2 hours, then purged in He for 30 min. After cooling down to RT, chemisorption was performed by pulse adsorption of 5 % CO in He at T = 24 °C. The metal dispersion was evaluated using stoichiometry of chemically adsorbed Pd/CO = 2/1 according to the eq. (3) (Section 2.2.2.5).

3.5. Catalytic performance in hydrogenation of 3-nitrotoluene

Model reaction for testing catalytic performance of prepared Pd@MWW catalysts was the hydrogenation of 3-nitrotoluene. Before the catalytic testing, each catalyst was firstly reduced in flow of H_2/N_2 at T = 450 °C (5 °C/min) for 4 hours (flow of H_2=116 ml/min, flow of N_2=110 ml/min). According to previous studies [67], the hydrogenation of 3-nitrotoluene was performed at T = 100 °C and partial pressure of H_2 3 bars. The 50 ml stainless steel reactor was filled with 35 ml of n-hexane as a solvent, 7.5 mmol of 3-nitrotoluene, 0.7 ml n-dodecane as an internal standard and 120 mg of a catalyst. The system was flushed with N_2 (30 bars) 3 times, then heated up to reaction temperature and by pressurizing the system with H_2 to ordinarily 4 bars, the reaction started.

Gas chromatography analysis of reaction mixture was performed by Agilent 7890B GC system with autosampler, FID detector, and a DB-5 column (30 m, 0,32 mm x 0,25 μm). The samples of the reaction mixture were taken after 1, 2, 4, 6 and 24 hours. The following conditions were used for analysis: V_{H2} = 40 ml/min, V_{air} = 450 ml/min, V_{N2} = 0.6 ml/min, $T_{detector}$ = 300 °C, $T_{injector}$ = 300 °C. Temperature program for column: 6 min at T = 60 °C, increasing the temperature with a ramp 30 °C/min to T = 250 °C. Analysis took 15 – 16 min, V_{sample} was 1 μl. The response factor of 3-NT (K_{3NT} = 1.413) was determined using internal standard calibration method and used for the evaluation the amount of a substrate as:

$$N_t = \frac{N_{IS}}{K\frac{A_{IS}}{A_t}} \quad (5)$$

where

N_t is the molar amount of 3-nitrotoluene at chosen time [mol];

N_{IS} is the molar amount of n-dodecane in reaction mixture[mol];

A_{IS} is the experimental area of chromatographic peak corresponding to n-dodecane [a.u.];

A_t is the experimental area of chromatographic peak corresponding to 3-nitrotoluene [a.u.];

K is the response factor of 3-nitrotoluene.

Conversion and initial reaction rate were calculated by following formulas:

- Conversion [%]$= \frac{N_0 - N_t}{N_0} * 100\%$ (6)
- Initial reaction rate [mol·g^{-1} $_{Pd}$·h^{-1}] $= \frac{conversion\ (at\ t=1h) * N_0}{100 * t * m_{Pd}}$ (7)

where N_0 – initial molar amount of 3-nitrotoluene [mol];

N_t – molar amount of 3-nitrotoluene at chosen time [mol];

t – reaction time, 1h;

m_{Pd} – mass of Pd in a catalyst sample [g].

4. Results and discussion

4.1. Physical-chemical characteristics of Pd@MWW catalysts

Modification of MCM-22P structure upon different post-synthesis treatments was analysed using X-ray diffraction (Figure 14, 15). The XRD patterns of MCM-22P(n) (Figure 14) show characteristic diffraction lines corresponding to the literature data.[68] The chemical composition of MCM-22P does not influence either intensities or the position of diffraction lines in XRD patterns. In particular, the diagnostic reflections at 2θ 6.5 ° (corresponding to d_{002} interlayer plane), 7.2 ° (d_{100}), 8.0 ° (d_{101}), 10.1 ° (d_{102}) were observed in all MCM-22P(n) samples.

The calcination of MCM-22P(n) resulted in removal of d_{002} interlayer reflection shifting to 2θ 7.1 ° and thus overlapped with d_{100} diffraction line at 7.2 ° in 3D MWW zeolite. In general, the prepared MWW(n) zeolites were characterised by three diagnostic reflections at 7.2 ° 2θ (12.3 Å d_{100}-spacing), 8.0 ° 2θ (11.0 Å d_{101}-spacing) and 10.0 ° 2θ (8.8 Å d_{102}-spacing)[6]. Thus, the XRD patterns of all MWW(n) samples corresponded to the reference pattern from IZA database.[2]

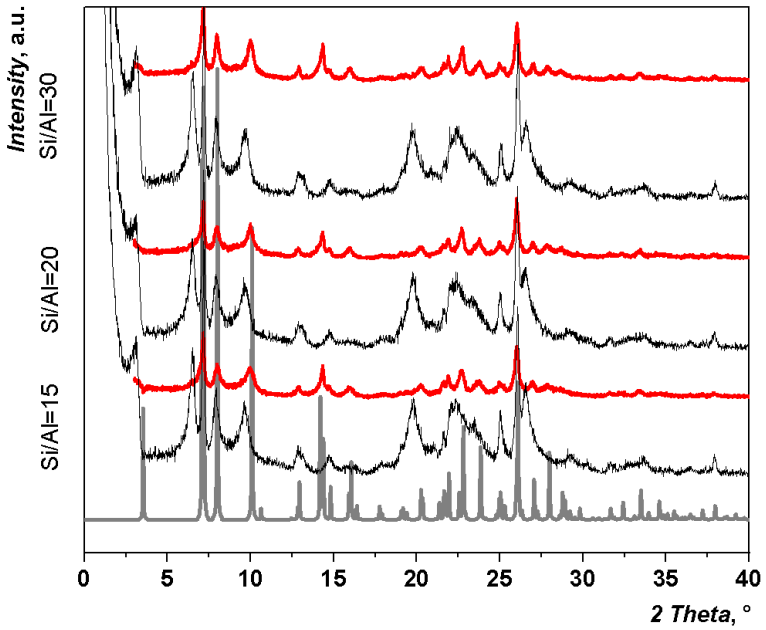

Figure 14: XRD diffractograms of MCM-22P(n) zeolites with different Si/Al ratios before (–) and after (–) calcination and also of reference MWW zeolite from IZA database (–)

Swelling of MCM-22P(n) combined with Pd impregnation resulted in several changes in the XRD patterns, further discussed for 0.1Pd@MWW(30)$_{2D\text{-}3D}$ sample

(Figure 15a). (i) The appearance of highly intensive 001 reflection at 2θ 3.0 ° in swollen MCM-22P(30) material indicated the successful expansion of the interlayer space upon treatment the respective layered zeolite precursor with CTMA-OH. (ii) The interlayer reflection 002 at 2θ 6.5 ° is shifted to the lower 2θ after the swelling as a consequence of increased layer spacing. (iii) The reflections 101 (8.0 ° 2θ, 11.0 Å d_{101}-spacing) and 102 (10.1 ° 2θ, 8.8 Å d_{102}-spacing) merged together, forming a broad peak in 8 ° - 10.1 ° region. All together the features (i) – (iii), observed upon swelling of all MCM-22P(n) materials with different Si/Al ratios, are diagnostic for complete swelling of MCM-22P precursor with $CTMA^+$.[69] In turn, the maintenance of the structure of zeolite layers in all swollen materials was confirmed by unaffected 220 (25 ° 2θ, 3.6 Å d-spacing) and 310 (26.1 ° 2θ, 3.4 Å d-spacing) reflections during swelling process.[70]

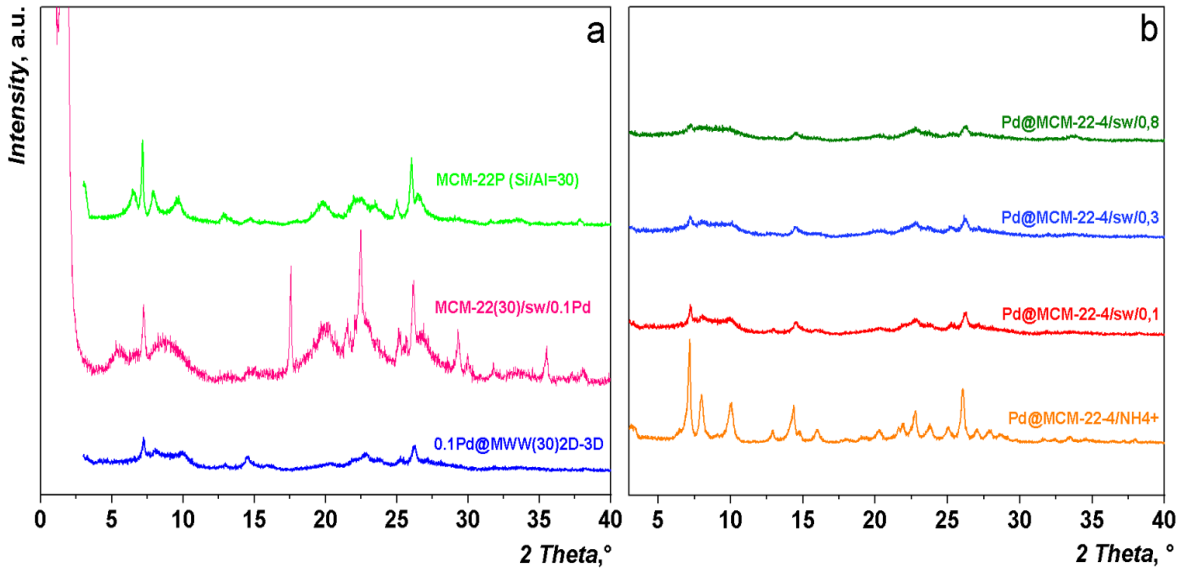

Figure 15: XRD diffractograms of (a) MCM-22P(30) (–), swollen MCM-22P(30) loaded with 0.1 wt.% Pd before (–) and after (–) calcination; (b) $0.1Pd@MWW(30)_{impreg}$ (–) $0.1Pd@MWW(30)_{2D\text{-}3D}$ (–), $0.3Pd@MWW(30)_{2D\text{-}3D}$ (–) and $0.8\ Pd@MWW(30)_{2D\text{-}3D}$ (–)

Figure 15b compares the XRD patterns of $0.1Pd@MWW(30)_{impreg}$ sample prepared by post-synthesis impregnation method with those of $xPd@MWW(30)_{2D\text{-}3D}$ materials with different metal loadings. Lower intensities of both interlayer and intralayer reflections for $0.1Pd@MWW(30)_{2D\text{-}3D}$ *vs.* $0.1Pd@MWW(30)_{impreg}$ indicate poor crystallinity (ordering) of the material prepared *via* '2D-3D incorporation' which may be explained by obstructed condensation of 2D layers in the presence of extra component (metal species). With increase

in the metal loading from 0.1 to 0.3 and 0.8 wt.%, condensation of layers becomes even more difficult due to the higher amount of MNPs located in the interlayer space of MCM-22P (Figure 15b). The same trend, i.e., decreasing ordering of a zeolite support with increase in the Pd loading, was also observed for xPd@ MWW(15)$_{2D-3D}$ and xPd@ MWW(20)$_{2D-3D}$ series.

4.2. ICP-MS

Si, Al and Pd content in Pd@MWW catalysts was determined by ICP-MS method (Table 3). For both Pd@MWW$_{impreg}$ and Pd@MWW$_{2D-3D}$ materials, the theoretical weight percentage of Pd in the samples estimated based on the Pd loading had only a little discrepancy with the experimentally found Pd content (e.g., 0.11 - 0.12 *vs.* 0.1 and 0.88 *vs.* 0.8 wt.% of Pd). This result confirms significantly improved efficiency of '2D-3D incorporation' method when the noble metal is loaded into the as-synthesized swollen zeolite (this work) rather than introduced upon the swelling of layered zeolite precursor (Ref.[41,42]). Thus, there were minimal losses of metal in all the synthesis steps (Section 3.3). Importantly, the benchmarking 0.1Pd@MWW$_{impreg}$ catalysts prepared *via* impregnation showed Pd contents being similar to 0.1Pd@MWW$_{2D-3D}$ samples prepared *via* '2D-3D incorporation' which enables further accurate comparative analysis of the catalytic performance of respective catalysts series.

Noticeably, Si/Al ratios in both Pd@MWW$_{impreg}$ and Pd@MWW$_{2D-3D}$ series closely resembled the ones used for the preparation of a zeolite support (Table 3). This result indicates a lack of framework atoms leaching upon the applied post-synthesis treatments (e.g., desilication in alkaline medium applied during swelling[25]).

Table 3: Si, Al and Pd content in Pd@MWW samples based on ICP-MS measurement *vs.* composition of reaction mixture

	Sample	Determined using ICP-MS		In reaction mixture	
		Si/Al, mol/mol	Pd content, wt.%	Pd loading, wt.%	Si/Al, mol/mol
1	0.1Pd@MWW(30) $_{impreg}$	22	0.08	0.1	30
2	0.1Pd@MWW(15) $_{impreg}$	13	0.07	0.1	15
3	0.1Pd@MWW(30)$_{2D-3D}$	21	0.12	0.1	30
4	0.1Pd@MWW(15)$_{2D-3D}$	11	0.11	0.1	15
5	0.1Pd@MWW(20)$_{2D-3D}$	19	0.12	0.1	20
6	0.8Pd@MWW(30)$_{2D-3D}$	21	0.88	0.8	30

4.3. Textural properties

The influence of the metal loading on the textural characteristics of Pd@MWW$_{2D-3D}$ catalysts was investigated using nitrogen physisorption. Figure 16 shows the typical ad-/ desorption isotherms for xPd@MWW(15)$_{2D-3D}$ series. Shape of the isotherms of xPd@MWW(15)$_{2D-3D}$ materials was similar to that of metal-free MWW(15) zeolite. Thus, all isotherms correspond to the type I(a) according to IUPAC classification, which reveals the micropore character of the designed catalysts. Analysis of the values of micropore volume (V_{mic}, Table 4) and BET area (S_{BET}, Table 4) determined using t-plot and BET method, respectively, indicated slight decreasing of respective characteristics by 5 – 10 % with increasing metal loading in the zeolite. This result can be explained by the encapsulation of MNPs in the void space of a zeolite resulted in partial filling the pores.

Table 4: Textural characteristics of MWW(15), 0.1Pd@MWW(15)$_{2D-3D}$, 0.3Pd@MWW(15)$_{2D-3D}$ and 0.8Pd@MWW(15)2D-3D samples

Sample	S_{BET} [m^2/g]	S_{ext} [m^2/g]	V_{mic} [cm^2/g]	V_{tot} [cm^2/g]
MWW(15)	500	123	0.17	0.36
0.1Pd@MWW(15)$_{2D-3D}$	485	152	0.15	0.39
0.3Pd@MWW(15)$_{2D-3D}$	467	143	0.15	0.36
0.8Pd@MWW(15)$_{2D-3D}$	442	135	0.14	0.36

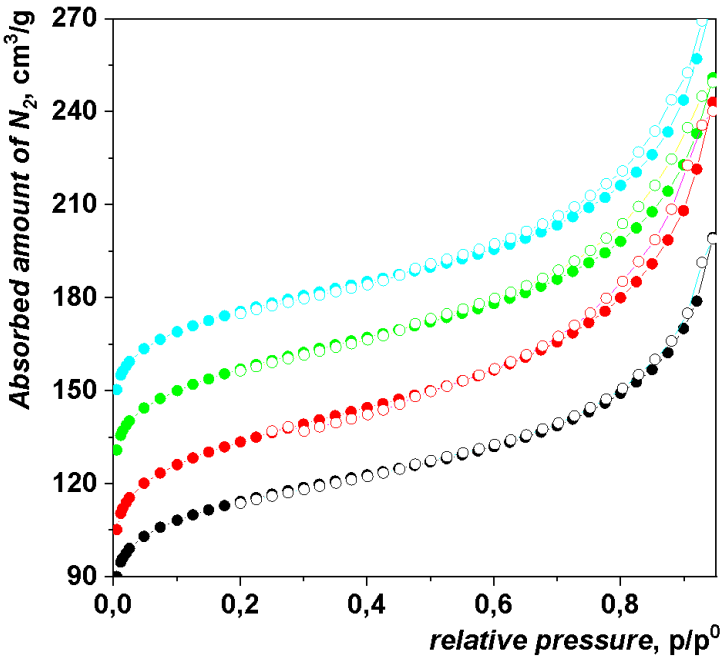

Figure 16: Nitrogen adsorption (•) and desorption (o) isotherms of MWW(15) (-), 0.1Pd@MWW(15)$_{2D\text{-}3D}$ (-), 0.3Pd@MWW(15)$_{2D\text{-}3D}$ (-) and 0.8Pd@MWW(15)$_{2D\text{-}3D}$ (-). Isotherms are shifted upwards for +15 (-), +40 (-) and +60 (-) for better visualization

4.4. FTIR of adsorbed pyridine

Investigation of the state of silanol groups and evaluation of the concentration of Brønsted and Lewis acid sites was performed using IR spectroscopy by analysing distinct regions of the spectra (Figure 17). The surface chemistry of the representative metal-free zeolite sample (MWW(30)) is further compared to that of xPd@MWW(30)$_{2D\text{-}3D}$ materials with different metal loadings. In the OH-region, the band of bridging -Si-(OH)-Al- (Brønsted acid sites) groups is observed at 3621 cm^{-1}. This band is the most intensive for metal-free MWW(30) zeolite. For the metal-loaded zeolites, the intensity of the band decreased ~3 times independently on the metal loadings. Both MWW(30) and xPd@MWW(30)$_{2D\text{-}3D}$ shows the intensive band of silanol groups on external surface at 3747 cm^{-1}. In addition, a small extra-band at 3733 cm^{-1} usually attributed to the internal silanol groups[71] is apparent for all xPd@MWW(30)$_{2D\text{-}3D}$ materials. The appearance of this band is in line with non-complete condensation of MCM-22P layered precursor even at minimal Pd loading (e.g., 0.1 wt.%)[42] also revealed by XRD (Section 4.1). Adsorption of pyridine, followed by thermodesorption at T = 150 °; 250 °; 350 ° and 450 °C was performed to determine the strength of acid sites (Figure 17b). The band 1544 cm^{-1} represents the adsorption of pyridine on the BAS, while the band at 1455 cm^{-1} corresponds to the interaction of probe molecule with Lewis acid sites;

the peak around 1490 cm^{-1} is related to the combination of pyridine absorbed on Brønsted and Lewis acid sites.

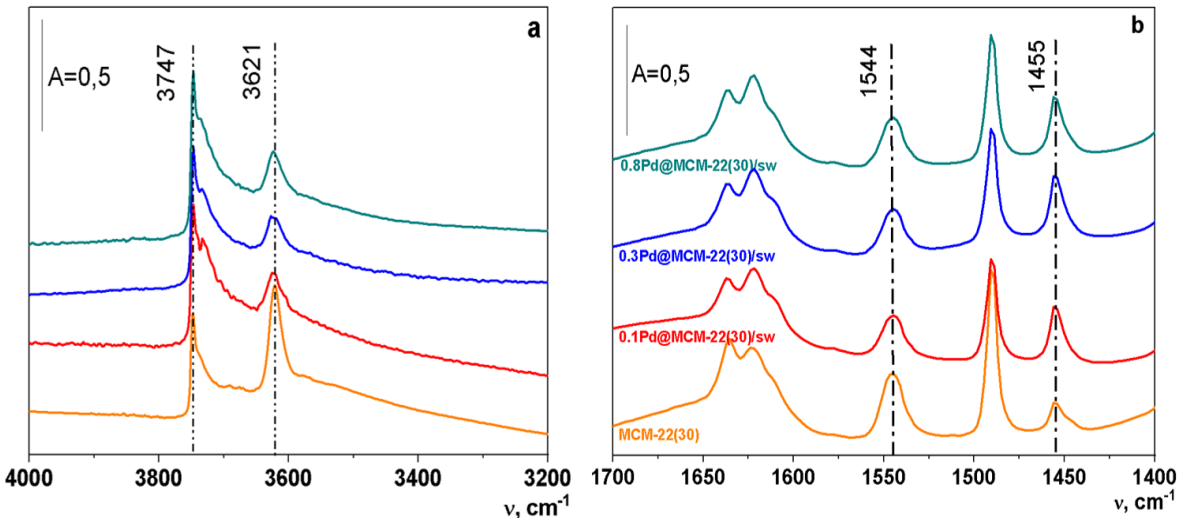

Figure 17: FTIR spectra of MWW(30) and xPd@MWW(30)$_{2D\text{-}3D}$ materials in (a) OH vibration region after activation at T=450 ºC; (b) pyridine ring vibration region after ad-/desorption of pyridine at T = 150 °C

The peak intensities provide information about the concentration of acid sites in catalysts of different Si/Al ratios and Pd loadings (Table 5). The concentration of both BAS and LAS decreases with increasing Si/Al ratio in a zeolite support (Table 5, entry 1-2) which is explained by the decreasing number of Al atoms in a zeolite framework. Noticeably, impregnation did not alter the concentration and ratio of BAS and LAS in a zeolite, while '2D-3D incorporation' led to decreasing fraction of BAS (entry 3-4). This result is in agreement with obstructed condensation of MCM-22P layers upon '2D-3D incorporation', which may prevent the conversion of Al Lewis acid sites (e.g., loosely bond framework $Al(OSi)_n$, $n < 4$) to bridging ≡Si-(OH)-Al≡ groups (i.e., Brønsted acid sites) with increasing the amount of Pd in the interlayer space indicated by the results of XRD (Section 4.1) and FTIR (Figure 17a). Together with determination of acidity, Si/Al ratio was determined based on the FTIR results and compared with results from ICP-MS (Table 5). It is observed that Si/Al ratio in a bulk material established by ICP-MS is slightly higher *vs.* the one determined using FTIR. The result, most likely, reflects the occurrence of some Al species in hexacoordinated form not contributing to either Brønsted or Lewis acidity.

Table 5: Concentrations of acid sites and respective Si/Al ratios in xPd@MWW samples determined using FTIR spectroscopy of adsorbed pyridine

	Sample	BAS, mmol/g	LAS, mmol/g	BAS+LAS, mmol/g	BAS/LAS	Si/Al FTIR	Si/Al ICP-MS
1	MWW(15)	0.40	0.15	0.55	2.7	21	n.d.*
2	MWW(30)	0.25	0.07	0.32	3.6	39	n.d.
3	0.1Pd@MWW(15) $_{impreg}$	0.36	0.13	0.49	2.8	24	13
4	0.1Pd@MWW(15)$_{2D-3D}$	0.30	0.14	0.44	2.1	26	11
5	0.1Pd@MWW(30)$_{2D-3D}$	0.21	0.12	0.33	1.8	34	21
6	0.3Pd@MWW(30)$_{2D-3D}$	0.18	0.13	0.31	1.4	35	n.d.
7	0.8Pd@MWW(30)$_{2D-3D}$	0.17	0.11	0.28	1.5	39	21

*n.d. – not determined

Figure 18 compares the results of pyridine thermodesorption for 0.1Pd@MWW(15)$_{impreg}$, 0.1Pd@MWW(15)$_{2D-3D}$, 0.1Pd@MWW(30)$_{2D-3D}$ and 0.8Pd@MWW(30)$_{2D-3D}$. samples. With the increasing desorption temperature, the concentration of pyridine adsorbed on acid sites decreases. At T = 450 °C only the complexes of pyridine with the strongest acid sites are present. The obtained distributions of acid sites according to their strength suggest similar fraction of strong acid centres, both Brønsted and Lewis, in Pd@MWW catalysts independently on the preparation method (e.g., impregnation or '2D-3D incorporation') or Pd loading. Slight increase in the concentration of LAS at T = 450 °C may be explained by the transformation of BAS to LAS at higher temperatures.

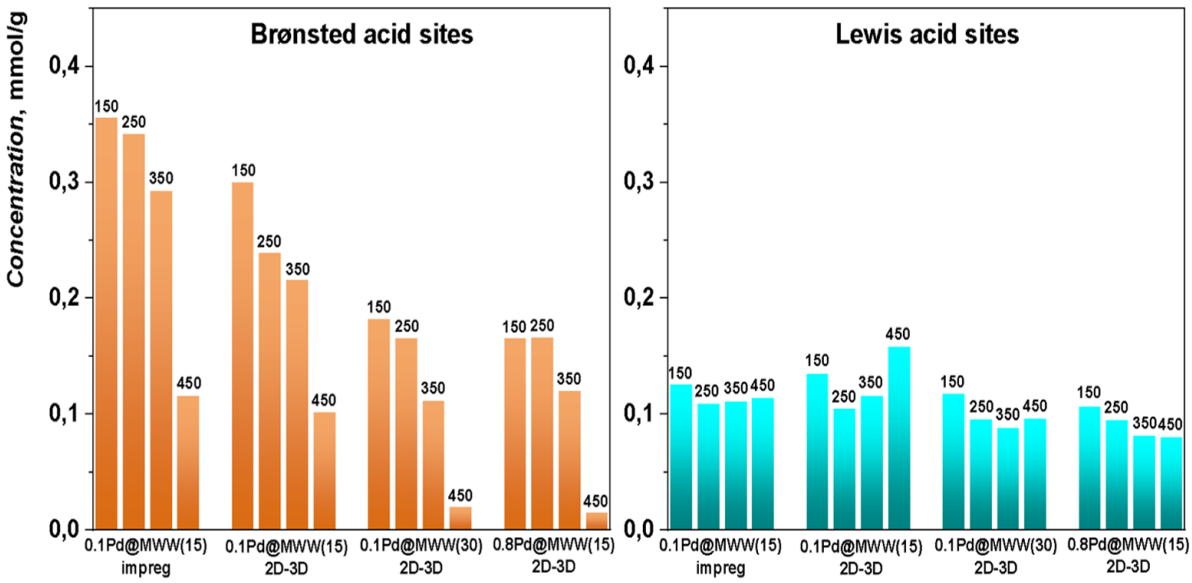

Figure 18: Distribution of acid sites according to their strength in Pd@MWW catalysts based on the results of pyridine thermodesorption monitored with FTIR spectroscopy

4.5. STEM and chemisorption

The Pd particle size distribution in Pd@MWW catalysts was investigated using STEM and CO chemosorption. White few-nm spots visible in representative STEM images (Figure 19) correspond to Pd particles. 0.8Pd@MWW(30)$_{2D\text{-}3D}$ (Figure 19a) with the highest metal loading apparently shows much larger particles in comparison to 0.3Pd@ MWW(30)$_{2D\text{-}3D}$ (Figure 19b) material, while only few sign of Pd was detected with STEM for 0.1Pd@MWW(30) $_{2D\text{-}3D}$ sample (Figure 19c). The latter result may be related to the particularly low loading and small size of Pd NPs in 0.1Pd@ MWW(30)$_{2D\text{-}3D}$ sample. Indeed, according to the CO chemisorption, more than a half of Pd atoms in 0.1Pd@ MWW(30)$_{2D\text{-}3D}$ were exposed on the surface (the dispersion D = 52.6 %). Noticeably, only 23.2 % of Pd occurs on the surface of metal NPs in 0.8Pd@MWW(30)$_{2D\text{-}3D}$, which is corresponding to STEM results (Figure 19a). In contrast to '2D-3D incorporated' 0.1Pd@ MWW(30)$_{2D\text{-}3D}$ sample, 0.1Pd@ MWW(30)$_{impreg}$ possessing the same Pd content showed 5-times lower dispersion (D = 11.2 %), which agrees with the presence of Pd in the form of large agglomerates seen in STEM images in Figure 19d.

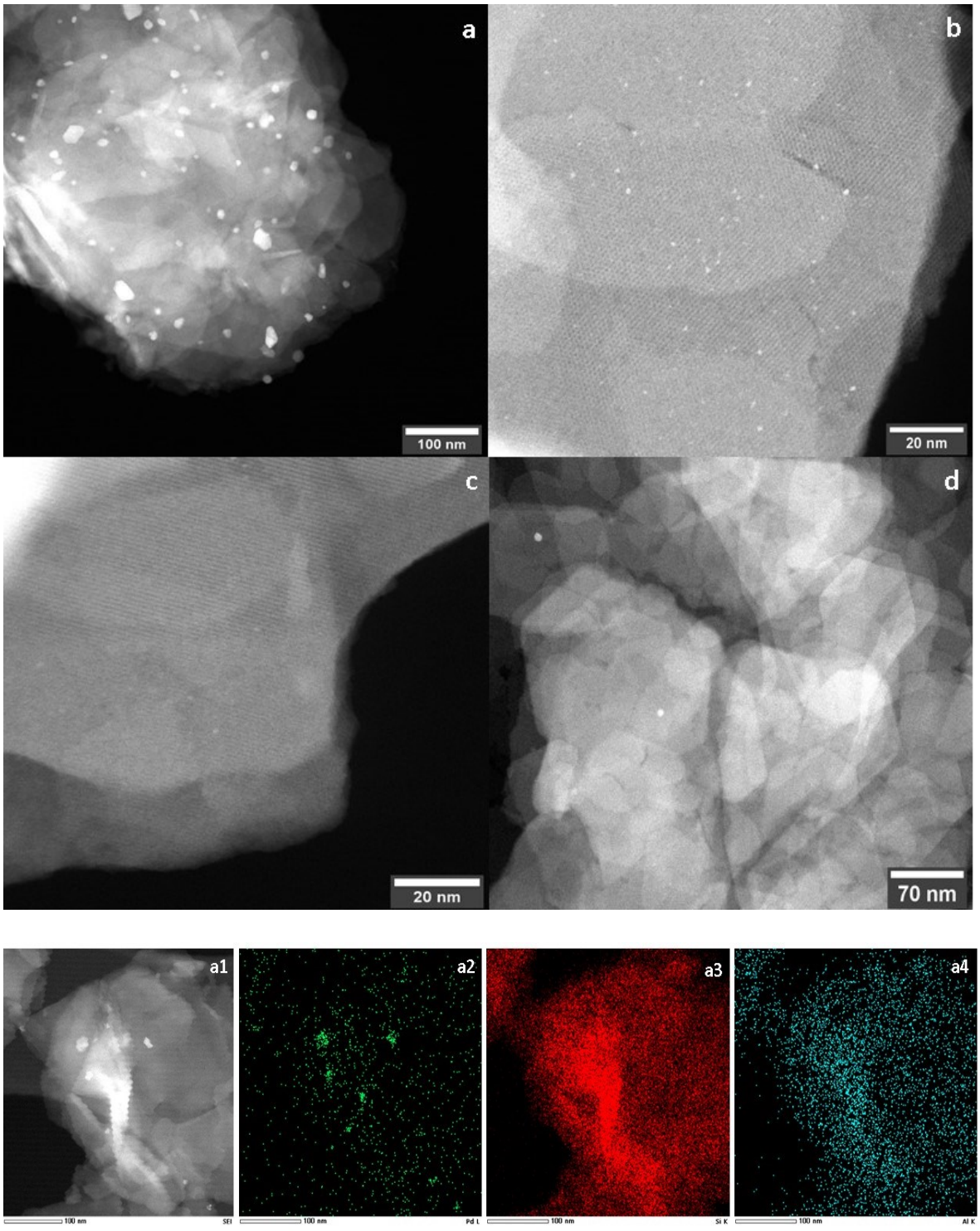

Figure 19: STEM images of 0.8Pd@MWW(30)$_{2D\text{-}3D}$ (a), 0.3Pd@MWW(30)$_{2D\text{-}3D}$ (b), 0.1Pd@MWW(30)$_{2D\text{-}3D}$ (c) and 0.1Pd@MWW(30)$_{impreg}$ (d) and EDS maps (a1-a4) for elemental distribution of Pd, Si and Al in 0.8Pd@MWW(30)$_{2D\text{-}3D}$ (a) sample, the elemental maps (a1-4) correspond to Pd (green), Si (red) and Al (blue) signals

Energy dispersive X-ray spectroscopy confirmed the presence of Pd in a form of clusters in 0.8Pd@MWW(30)$_{2D\text{-}3D}$ sample, while zeolite framework silicon and aluminium atoms are evenly distributed in the sample (Figure 19a1-4).

The Pd nanoparticle size in 0.3Pd@MWW(30)$_{2D\text{-}3D}$ and 0.8Pd@MWW(30)$_{2D\text{-}3D}$ is further specified in particle size distribution histograms (Figure 20) obtained by detailed analysis of respective STEM images. The average size of MNPs in 0.3Pd@MWW(30)$_{2D\text{-}3D}$ corresponds to 1.14 nm, while 0.8Pd@MWW(30)$_{2D\text{-}3D}$ shows much broader particle size distribution centred at 8.35 nm. The obtained results may indicate the occurrence of a substantial fraction of Pd NPs on the external surface of 0.8Pd@MWW(30)$_{2D\text{-}3D}$ sample. Noticeably, the average size of Pd MNPs encapsulated to MWW(15) framework at 0.79 wt.% *via* non-modified '2D-3D incorporation' approach (e.g., metal loading during swelling treatment) was only slightly higher (1.9 nm) in comparison to 0.3Pd@MWW(30)$_{2D\text{-}3D}$.[42]

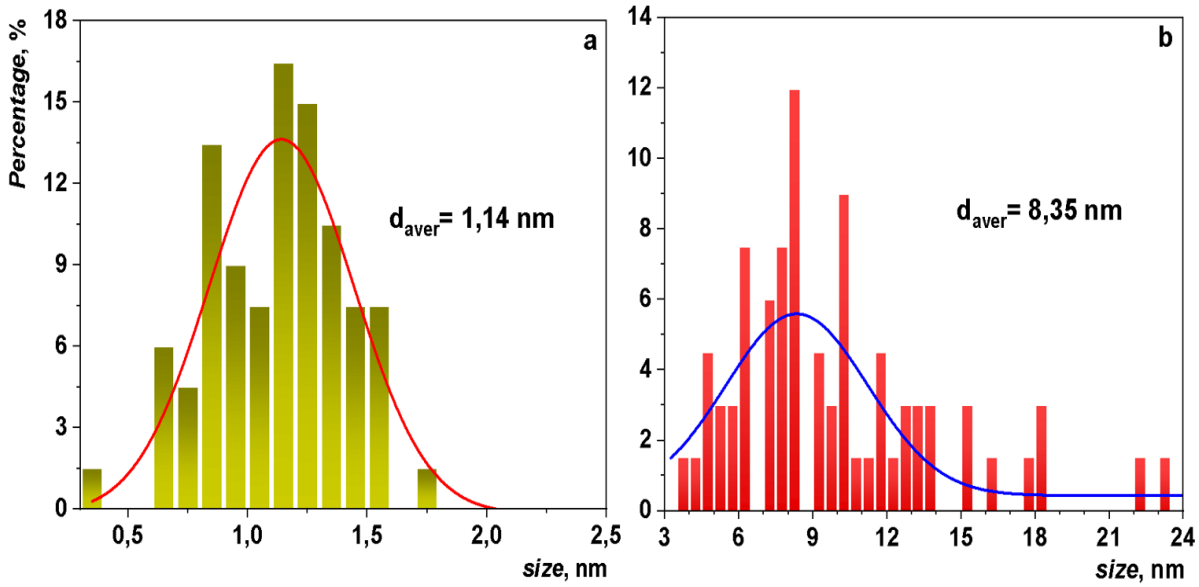

Figure 20: Pd nanoparticle size distribution graph of 0.3Pd@MWW(30)$_{2D\text{-}3D}$ (a) and 0.8Pd@MWW(30)$_{2D\text{-}3D}$ (b) with their average nanoparticle size

4.6. Catalytic performance

Catalytic testing of representative Pd@MWW samples was performed using hydrogenation of 3-nitrotoluene as a model reaction. Pd@MWW materials prepared by different methods and having different metal loading all showed 100% selectivity to 3-aminotoluene, but differed in 3-NT conversion (Table 6). The highest conversion (51 % after 1 hour TOS) was reached using 0.8Pd@MWW(30)$_{2D\text{-}3D}$ catalyst prepared *via* '2D-3D incorporation'.

Noticeably, 0.3Pd@MWW(30)$_{2D-3D}$ exhibited similar to 0.8Pd@MWW(30)$_{2D-3D}$ conversion value (49 %) despite substantial decrease in a content of active Pd phase. The maintenance of the conversion value with increasing metal loading in 0.8Pd@MWW(30)$_{2D-3D}$ is, most likely, caused by the non-optimum size of Pd aggregates in 0.8Pd@MWW(30)$_{2D-3D}$ (Figure 19a), which, according to STEM, are too large and thus there is only relatively small fraction of surface metal atoms available for catalysis. In line with poor dispersion of Pd NPs in impregnated 0.1Pd@MWW(30)$_{impreg}$ sample, the conversion of 3-nitrotoluene over 0.1Pd@MWW(30)$_{impreg}$ after 1 hour TOS totalled only 4 %. In contrast, '2D-3D impregnated' 0.1Pd@MWW(30)$_{2D-3D}$. with the same metal loading but better dispersed Pd phase showed 34 % conversion of 3-NT.

Table 6: Catalytic results for hydrogenation of 3-NT over differently synthesised Pd@MCM-22 catalysts

	Sample	Conversion 1h [%]	Selectivity to 3-aminotoluene	Initial rate [$mol_{3\text{-}NT} \cdot g^{-1}_{Pd} \cdot h^{-1}$]
1	0.8Pd@MWW(30)$_{2D-3D}$	51		3.7
2	0.3Pd@MWW(30)$_{2D-3D}$	49		9.6
3	0.1Pd@MWW(30)$_{2D-3D}$	34	100%	20.2
4	0.1Pd@MWW(20)$_{2D-3D}$	35		21.2
5	0.1Pd@MWW(30)$_{impreg}$	4		2.0
6	Pd@MWW (Ref. [42])	n.d.*		8.9

*n.d. – not determined

The designed catalysts can be further differentiated based on the initial reaction rate values normalized by the weight of active Pd component (Table 6). In a series of xPd@MWW(30)$_{2D-3D}$ samples, the normalized initial reaction rate decreased with increasing metal loading, x, as follows: 0.1 (21.2 $mol_{3\text{-}NT} \cdot g^{-1}_{Pd} \cdot h^{-1}$) >> 0.3 (9.6 $mol_{3\text{-}NT} \cdot g^{-1}_{Pd} \cdot h^{-1}$) >> 0.8 (3.7 $mol_{3\text{-}NT} \cdot g^{-1}_{Pd} \cdot h^{-1}$). This sequence well correlates with decreasing the fraction of exposed Pd surface atoms, verified by STEM and chemisorption results (Section 4.4). As confirmed by STEM images (Figure19a), the least active among '2D-3D impregnated' catalyst 0.8Pd@MWW(30)$_{2D-3D}$ possesses bulk Pd aggregates with limited number of surface Pd atoms reachable for the reacting molecules.

Importantly, the initial reaction rates achieved over 0.1Pd@$MWW_{2D\text{-}3D}$ catalysts synthesized *via* "modified" '2D-3D incorporation' method (Table 6, entry 3-4) were somewhat higher in comparison to the previously reported Pd@MWW material (Table 6, entry 6) prepared according to the pioneering synthesis protocol[42], which suffers from significant noble metal loss (0.79 wt.% of Pd in the sample *vs.* 4 wt.% loaded). In turn, comparable activities of 0.1Pd@$MWW(n)_{2D\text{-}3D}$ catalysts with various Si/Al ratios (Table 6, entry 3-4) suggest the potential of '2D-3D incorporation' synthesis protocol for the preparation of efficient bifunctional metal-supported zeolite catalysts with variable concentrations of acid sites.

5. Conclusions

Development of cost-efficient synthetic methods enabling stabilization of noble metal nanoparticles on zeolite supports for the preparation of active, selective and durable mono- and bifunctional catalysts has been in the focus of recent research activities. Recently emerged synthetic approach based on the transformation of MCM-22P layered zeolite precursor into 3D framework coupled with metal impregnation ('2D-3D incorporation') appeared as a breakthrough strategy for the preparation of nanometric particles of noble metals (i.e., Pt and Pd) well-dispersed in acid sites-free pure silica MWW zeolite. This study aimed at further development of '2D-3D incorporation' method towards preparation of bifunctional acid-metal Pd@MWW catalysts with tuneable concentration of acid sites.

The Pd-supported MWW zeolites with Si/Al ratios 15, 20, 30 and Pd loadings varying in the range 0.1 – 0.8 wt.% were prepared using either '2D-3D incorporation' or conventional impregnation. The textural and structural properties of the catalysts were investigated by X-ray diffraction and nitrogen physisorption, respectively, while transmission electron microscopy and CO chemisorption provided information about size and dispersion of Pd MNPs. Infrared spectroscopy allowed to assess the nature, concentration and strength of acid sites in the prepared Pd@MWW catalysts. Chemical analysis confirmed the quantitative loading of Pd into MWW zeolites *via* '2D-3D incorporation' modified by separation of swelling and metal impregnation steps in time. The catalytic activity of thus prepared and characterized Pd@MWW samples was investigated in a model reaction of hydrogenation of 3-nitrotoluene to 3-aminotoluene.

Incorporation of Pd was proved to be more effective by 2D-3D transformation, where Pd MNPs were trapped between crystalline zeolite layers after calcination of the swollen precursor. The increasing metal loading upon '2D-3D incorporation' caused

- incomplete condensation of zeolite layers (according to XRD);
- lower metal dispersion on the external surface and appearance bulk metal aggregates (confirmed by STEM analysis and CO chemisorption);
- insignificant decrease (5 – 10 %) of micropore volume in comparison to metal-free zeolite support (according to nitrogen physisorption);
- decrease in the fraction of Brønsted acid sites (~2 times for Pd loadings 0.1 – 0.8 wt.%) in comparison to metal-free zeolite support (according to FTIR spectroscopy of adsorbed pyridine).

The Pd@MWW samples prepared by ‘2D-3D incorporation’ were characterized by higher dispersion of Pd species (dispersion 50 % at Pd loading 0.1 wt.%) encapsulated into zeolite internal voids if to compare with the catalysts prepared *via* conventional impregnation method (dispersion 11% at Pd loading 0.1 wt.%). Consistently, the former catalysts were remarkably more active in the model reaction of 3-nitrotoluene hydrogenation, showing ~10 times higher values of initial reaction rates normalized by the weight of Pd. The dispersion of Pd in ‘2D-3D impregnated’ Pd@MWW catalysts and their hydrogenation activity were not affected by Si/Al ratio of a zeolite support, but decreased with increasing Pd loading from 0.1 to 0.8 wt.%. The obtained results reveal the versatility of ‘2D-3D incorporation’ for the development of highly active hydrogenation catalysts with variable concentration of acid sites. In future, it would be interesting to focus on developing the fine dispersion of MNPs and prevent the formation of metal aggregates, by improvement of the method for metal loading in a zeolite precursor.

6. List of references

1. Čejka, J.; Žilková, N.: Syntéza a struktura zeolitů. *Chem. List.* **94**, 278–287 (2000).
2. Ch. Baerlocher, CH.; McCusker, L.B.; Meier, W.M.; Olson, D.H.: *Database of Zeolite Structures*. Available from URL: <http://www.iza-structure.org/databases/> [cit.28.11.2020]
3. Król, M.: Natural vs. Synthetic zeolites. *Crystals* **10**, 1–8 (2020).
4. Wang, S.; Peng, Y.: Natural zeolites as effective adsorbents in water and wastewater treatment. *Chem. Eng. J.* **156**, 11–24 (2010).
5. Čejka, J.; Morris, R. E.; Nachtigall, P.: *Zeolites in Catalysis: Properties and Applications*. Cambridge, The Royal Society of Chemistry 2017.
6. Čejka, J.; Bekkum, H. van; Corma, A. et al.: *Introduction to zeolite science and practice*. Oxford, Elsevier 2007.
7. Mgbemere, H. E.; Ekpa, I. C.; Lawal, G. I.: Zeolite Synthesis, Characterisation and Application Areas: A Review. *Int. Res. J. Environ. Sci.* **6**, 45–59 (2017).
8. Shamzhy, M.; Opanasenko, M.; Concepcion, P. et al.: New trends in tailoring active sites in zeolite-based catalysts. *Chem. Soc. Rev.* **48**, 1095–1149 (2019).
9. Aiello, R.; Nagy, J. B.; Giordano, G. et al.: Isomorphous substitution in zeolites. *Comptes Rendus Chim.* **8**, 321–329 (2005).
10. Díaz, U.; Corma, A.: Layered zeolitic materials: An approach to designing versatile functional solids. *Dalt. Trans.* **43**, 10292–10316 (2014).
11. Davis, M. E.: The quest for extra-large pore, crystalline molecular sieves. *Chem. - A Eur. J.* **3**, 1745–1750 (1997).
12. Weingarten, R.; Tompsett, G. A.; Curtis, C. et al.: Design of solid acid catalysts for aqueous-phase dehydration of carbohydrates : The role of Lewis and Brønsted acid sites. *J. Catal.* **279**, 174–182 (2011).
13. De, S.; Dutta, S.; Saha, B.: Critical design of heterogeneous catalysts for biomass valorization: current thrust and emerging prospects. *Catal. Sci. Technol.* **6**, 7364–7385 (2016).
14. Kloprogge, J. T.; Ruan, H. D.; Frost, R. L.: Thermal decomposition of bauxite minerals: Infrared emission spectroscopy of gibbsite, boehmite and diaspore. *J. Mater. Sci.* **37**, 1121–1129 (2002).
15. Cundy, C. S.; Cox, P. A.: The hydrothermal synthesis of zeolites : Precursors , intermediates and reaction mechanism. *Microporous Mesoporous Mater.* **82**, 1–78 (2005).
16. Grand, J.; Awala, H.; Mintova, S.: Mechanism of zeolites crystal growth: New findings and open questions. *CrystEngComm* **18**, 650–664 (2016).
17. Sánchez, M.; Díaz, R. D.; Córdova, T. et al.: Microporous and Mesoporous Materials Study of template interactions in MFI and MEL zeolites using quantum methods.

Microporous Mesoporous Mater . **203**, 91–99 (2015).

18. Cundy, C. S.; Cox, P. A.: The hydrothermal synthesis of zeolites: History and development from the earliest days to the present time. *Chem. Rev.* **103**, 663–701 (2003).

19. Maldonado, M.; Oleksiak, M. D.; Chinta, S. etal.: Controlling crystal polymorphism in organic-free synthesis of na-zeolites. *J. Am. Chem. Soc.* **135**, 2641–2652 (2013).

20. Zhang, K.; Ostraat, M. L.: Innovations in hierarchical zeolite synthesis. *Catal. Today* **264**, 3–15 (2016).

21. Choi, M.; Na, K.; Kim, J. et al.: Stable single-unit-cell nanosheets of zeolite MFI as active and long-lived catalysts. *Nature* **461**, 246–249 (2009).

22. Schreyeck, L.; Caullet, P.; Mougenel, J. C. et al.: PREFER: A new layered (alumino) silicate precursor of FER-type zeolite. *Microporous Mater.* **6**, 259–271 (1996).

23. Opanasenko, M. V.; Roth, W. J.; Čejka, J.: Two-dimensional zeolites in catalysis: Current status and perspectives. *Catal. Sci. Technol.* **6**, 2467–2484 (2016).

24. Kikhtyanin, O.; Chlubná, P.; Jindrová, T. et al.: Peculiar behavior of MWW materials in aldol condensation of furfural and acetone. *Dalton Trans.* **43**, 10628–10641 (2014).

25. Roth, W. J.; Čejka, J.; Millini, R. et al.: Swelling and Interlayer Chemistry of Layered MWW Zeolites MCM-22 and MCM-56 with High Al Content. *Chem. Mater.* **27**, 4620–4629 (2015).

26. Roth, W. J.; Nachtigall, P.; Morris, R. E. et al.: Two-dimensional zeolites: Current status and perspectives. *Chem. Rev.* **114**, 4807–4837 (2014).

27. Schoonheydt, R. A.; Pinnavaia, T.; Lagaly, G. et al.: Pillared clays and pillared layered solids. *Pure Appl. Chem.* **71**, 2367–2371 (1999).

28. Csicsery, S. M.: Shape-selective catalysis in zeolites. *Zeolites* **4**, 116–126 (1984).

29. Teketel, S.; Erichsen, M.W.; Bleken, F.L. et al.: Shape selectivity in zeolite catalysis. The Methanol to Hydrocarbons (MTH) reaction. *Catalysis* **26**, 179–217 (2014).

30. Bae, J.; Cichocka, M.O.; Zhang, Y. et al.: Phase Transformation Behavior of a Two-Dimensional Zeolite. *Angew. Chemie - Int. Ed.* **58**, 10230–10235 (2019).

31. Schulman, E.; Wu, W.; Liu, D.: Two-Dimensional Zeolite Materials: Structural and Acidity Properties. *Materials.* **13**, 1822–1874 (2020).

32. Goursot, A.; Vasilyev, V.; Arbuznikov, A.: Modeling of Adsorption Properties of Zeolites : Correlation with the Structure. *J. Phys. Chem. B* **101**, 6420–6428 (1997).

33. Khosravi, A.; Esmhosseini, M.; Khezri, S.: Removal of ammonium ion from aqueous solutions using natural zeolite: Kinetic, equilibrium and thermodynamic studies. *Res. Chem. Intermed.* **40**, 2905–2917 (2014).

34. Wang, N.; Sun, Q.; Yu, J.: Ultrasmall Metal Nanoparticles Confined within Crystalline Nanoporous Materials: A Fascinating Class of Nanocatalysts. *Adv. Mater.* **31**, 1–23 (2019).

35. Goel, S.; Wu, Z.; Zones, S. I. et al.: Synthesis and catalytic properties of metal clusters

encapsulated within small-pore (SOD, GIS, ANA) zeolites. *J. Am. Chem. Soc.* **134**, 17688–17695 (2012).

36. Zaarour, M.; Cazemier, J.; Ruiz-Martínez, J.: Recent developments in the control of selectivity in hydrogenation reactions by confined metal functionalities. *Catal. Sci. Technol.* **10**, 8140–8172 (2020).

37. Peron, D. V.; Zholobenko, V.L.; Rocha, M.R. et al.: Nickel – zeolite composite catalysts with metal nanoparticles selectively encapsulated in the zeolite micropores. *J. Mater. Sci.* **54**, 5399–5411 (2019).

38. Weckhuysen, B. M.; Wang, D.; Rosynek, M. P. et al.: Conversion of Methane to Benzene over Transition Metal Ion ZSM-5 Zeolites. *J. Catal.* **175**, 338–346 (1998).

39. Chupin, J.; Gnep, N. S.; Lacombe, S. et al.: Influence of the metal and of the support on the activity and stability of bifunctional catalysts for toluene hydrogenation. *Appl. Catal. A Gen.* **206**, 43–56 (2001).

40. Stolz, C.; Sauvage, A.; Massiani, P. et al.: Solid-state exchange of palladium in zeolite NaX. *Appl. Catal. A Gen.* **167**, 113–121 (1998).

41. Liu, L.; Diaz, U.; Arenal, R. et al.: Generation of subnanometric platinum with high stability during transformation of a 2D zeolite into 3D. *Nat. Mater.* **16**, 132–138 (2017).

42. Zhang, Y.; Fulajtarova, K.; Kubu, M. et al.: Controlling dispersion and accessibility of Pd nanoparticles via 2D-to-3D zeolite transformation for shape-selective catalysis: Pd@MWW case. *Mater. Today Nano* **8**, 1–12 (2019).

43. Giannini, C.; Ladisa, M.; Altamura, D. et al.: X-ray Diffraction : A Powerful Technique for the Multiple-Length-Scale Structural Analysis of Nanomaterials. *Crystals* **6**, 1–22 (2016).

44. Cychosz, K. A.; Guillet-Nicolas, R.; Garcia-Martinez, J. et al.: Recent advances in the textural characterization of hierarchically structured nanoporous materials. *Chem. Soc. Rev.* **46**, 389–414 (2017).

45. Bordiga, S.; Lamberti, C.; Bonino, F., et al.: Probing zeolites by vibrational spectroscopies. *Chem. Soc. Rev.* **44**, 7262–7341 (2015).

46. Rainer, D. N.; Mazur, M.: Electron microscopy methods for characterisation of zeolite catalysts. *Catalysis* **32**, 151–187 (2020).

47. Sarkany, J.; Gongalez, R.: On the Use of the Dynamic Pulse Method to Measure Metal Surface Areas. *J. Catal.* **76**, 75–83 (1982).

48. Speakman, S. *Basics of X-Ray Powder Diffraction*. Available from URL: http://prism.mit.edu/xray/documents/1%20Basics%20of%20X-Ray%20Powder%20Diffraction.pdf [cit.22.3.2021]

49. Guinier, A.: X-Ray Diffraction: In Crystals, Imperfect Crystals, and Amorphous Bodies. *J. Chem. Educ.* **41**, 292 (1964).

50. Poly Crystallography: *An Introduction to X-ray Powder Diffraction Analysis*. Available from URL: <http://www.polycrystallography.com/XRDanalysis.html> [cit.2.4.2021]

51. Particle Technology Labs: *Micropore and Mesopore Measurement.* Available from URL: <https://www.particletechlabs.com/analytical-testing/gas-adsorption-and-porosimetry/micropore-measurement> [cit.2.4.2021]

52. Sultan, M.; Miyazaki, T.; Koyama, S.: Optimization of adsorption isotherm types for desiccant air-conditioning applications. *Renew. Energy* **121**, 441–450 (2018).

53. Inkson, B. J.: Scanning electron microscopy (SEM) and transmission electron microscopy (TEM) for materials characterization. In: *Materials Characterization Using Nondestructive Evaluation (NDE) Methods.* Duxford: Elsevier , p.17–43, 2016.

54. Shustorovich, E.: Chemisorption phenomena: Analytical modeling based on perturbation theory and bond-order conservation. *Surf. Sci. Rep.* **6**, 1–63 (1986).

55. Nandiyanto , A.B.D.; Girsang, G.C.S.; Maryanti, R. et al.: Isotherm adsorption characteristics of carbon microparticles prepared from pineapple peel waste. *Commun. Sci. Technol.* **5**, 31–39 (2020).

56. Quantachrome Instruments: *TPR / TPD ChemBET Pulsar Automatic Chemisorption Analyzer*, User manual

57. Wedler, G.: *Chemisorption: An Experimental Approach*. London, Butterworths 1976.

58. Bergeret, G.; Gallezot, P.: Particle Size and Dispersion Measurements. in *Handbook of Heterogeneous Catalysis*. Weinheim: Wiley-VCH, p.439–464, 2008.

59. Canton, P.; Fagherazzi, G.; Battagliarin, M. et al.: Pd/CO average chemisorption stoichiometry in highly dispersed supported Pd/γ-Al2O3 catalysts. *Langmuir* **18**, 6530–6535 (2002).

60. Anjalin, M.; Kanagathara, N.; Suganthi, B.A.R.: A brief review on aniline and its derivatives. *Mater. Today Proc.* **33**, 4751–4755 (2020).

61. Jagadeesh, V.; R., Surkus, A.-E.; Junge, H. et al.: Nanoscale Fe2O3-Based Catalysts for Selective Hydrogenation of Nitroarenes to Anilines. *Science (80).* **342**, 1073–1076 (2013).

62. Serna, P.; Corma, A.: Transforming Nano Metal Nonselective Particulates into Chemoselective Catalysts for Hydrogenation of Substituted Nitrobenzenes. *ASC Catal.* **5**, 7114–7121 (2015).

63. Rouquerol, F.; Rouquerol, J.; Sing, K. S. W. et al.: *Adsorption by Powders and Porous Solids: Principles, Methodology and Application*. London, Academic Press 2014.

64. Lowell, S.; Shields, J. E.; Thomas, M. A. et al.: *Characterization of porous solids and powders: surface area, pore size, and density*. Dordrecht, Kluwer Academic Publishers 2004.

65. Lippens, B. C.; Boer, J. H.: Studies on pore systems in catalysts. *J. Catal.* **4**, 319–323 (1965).

66. Barrett, E. P.; Joyner, L. G.; Halenda, P. P.: The Determination of Pore Volume and Area Distributions in Porous Substances. I. Computations from Nitrogen Isotherms. *J. Am. Chem. Soc.* **73**, 373–380 (1951).

67. Emeis, C. A.: Determination of Integrated Molar Extinction Coefficients for IR

Absorption Bands of Pyridine Adsorbed on Solid Acid Catalysts. *J. Catal.* **24**, 347–354 (1993).

68. Zhang, Y.; Fulajtarova, K.; Kubu., M. et al.: Electronic/steric effects in hydrogenation of nitroarenes over the heterogeneous Pd@BEA and Pd@MWW catalysts. *Catal. Today* **345**, 39–47 (2020).

69. Roth, W. J.; Dorset, D. L.: Expanded view of zeolite structures and their variability based on layered nature of 3-D frameworks. *Microporous Mesoporous Mater.* **142**, 32–36 (2011).

70. Roth, W. J.; Dorset, D. L.; Kennedy, G. J.: Discovery of new MWW family zeolite EMM-10: Identification of EMM-10P as the missing MWW precursor with disordered layers. *Microporous Mesoporous Mater.* **142**, 168–177 (2011).

71. Maheshwari, S.; Edgar, J.; Sandeep, K. et al.: Layer Structure Preservation during Swelling, Pillaring, and Exfoliation of a Zeolite Precursor. *J. Am. Chem. Soc.* **130**, 1507–1516 (2008).

72. Hadjiivanov, K.: Identification and Characterization of Surface Hydroxyl Groups by Infrared Spectroscopy. *Adv. Catal.* **57**, 99–318 (2014).